

Characterization and mapping of surface physical properties of Mars from CRISM multi-angular data: application to Gusev Crater and Meridiani Planum

J. Fernando^{1,2}, F. Schmidt^{1,2}, C. Pilorget³, P. Pinet^{4,5}, X. Ceamanos⁶, S. Douté⁷, Y. Daydou^{4,5}, F. Costard^{1,2}

¹Univ. Paris-Sud, GEOPS, UMR 8148, Orsay, 91405, France ²CNRS, Orsay, 91405, France, jennifer.fernando@u-psud.fr
³Division of Geological and Planetary Sciences, Caltech, Pasadena, California, USA ⁴Univ. de Toulouse, UPS-OMP, Toulouse, France ⁵CNRS, IRAP, Toulouse, France ⁶Météo France/CNRS, CNRM/GAME, Toulouse, France, ⁷Univ. Joseph Fourier/CNRS, IPAG, Grenoble, France

Abstract

The analysis of the surface texture from the particle (grain size, shape and internal structure) to its organization (surface porosity and roughness) provides information on the geological processes which formed and modified the planetary surfaces. CRISM multi-angular observations (varied emission angles) allow to characterize the surface scattering behavior which depends on the composition but also the material physical properties such as the grain size, shape, internal structure, and the surface roughness. After an atmospheric correction (compensating mineral aerosol effects) by the Multi-angle Approach for Retrieval of the Surface Reflectance from CRISM Observations (MARS-ReCO), the surface reflectances at different geometries are analyzed by inverting the Hapke's photometric model depending on six parameters: single scattering albedo, 2-term phase function, macroscopic roughness and 2-term opposition effects parameters. In the present work, surface photometric maps are created to observe the spatial variations of surface scattering properties as a function of geological units. Information on the single scattering albedo, the particle phase function and the macroscopic roughness are provided at the CRISM spatial resolution (200m/pixel). The article is an application of the methodology on the Mars Exploration Rover (MER) landing sites located at Gusev Crater and Meridiani Planum where orbital and in situ observations are available. Complementary orbital observations (e.g. CRISM spectra, THERMAL EMISSION IMAGING SYSTEM (THEMIS), High Resolution Imaging Science Experiment, (HiRISE)/MRO images) are used for interpreting the estimated Hapke photometric parameters in terms of physical properties, providing useful information on the geological processes. The in situ observations are used as ground truth to validate the interpretations. Varied scattering properties are observed inside a CRISM observation (5x10km) suggesting that the surfaces are controlled by local geological processes (e.g. volcanic resurfacing, aeolian and impact processes) rather than regional or global. We demonstrate that the macroscopic roughness parameter provides quantitative information on the surface roughness from millimeter- to centimeter-scales, useful for the selection of the next rover landing sites due to engineering constraints on the landing and the trafficability. Consistent results with the in situ observations are observed thus validating the approach and the use of photometry for the characterization of Martian surface physical properties.

Citation: Fernando, J. et al. (2014), Characterization and mapping of surface physical properties of Mars from CRISM multi-angular data: application to Gusev Crater and Meridiani Planum, in revision, Icarus

1 Introduction

The geological and climatic processes, such as external (e.g., space weathering), internal processes (e.g., volcanism) and interaction between surface and atmosphere (e.g., aqueous and wind erosions, alterations, transportations and depositions, CO₂ and H₂O cycles), have modified the planetary surfaces. These processes are recorded in the surface mineralogy and the surface texture. The mineral assemblage gives information on the chemical environment (e.g., crystallization from an igneous magma, deposition from aqueous agents, recrystallization due to metamorphism, crystallization during diagenesis process of sediments, oxidation and weathering of rocks due to interactions with the atmosphere). The analyses of the surface texture from the particle (grain size, shape and internal structure) to its organization (surface porosity and roughness) provide information on the surface formation (e.g., the grain size discriminates volcanic and plutonic materials), the transportation (e.g., the grain shape informs on the origin of the transportation and/or the capability of the erosion agent (liquid or wind) to erode the grains), the deposition and the weathering and thus in their evolution.

Photometry, through the measurement of the bidirectional reflectance in visible and near-infrared ranges at different geometries (incidence, emission and azimuthal angles), provides information on the scattering behavior. This scattering depends on the composition but also the material physical properties: from the particle scale such as its size, shape, internal structure to its organization inside a pixel such as surface roughness. This technique was already used for the analysis of laboratory measurements (e.g. *McGuire and Hapke*, 1995; *Piatek et al.*, 2004; *Cord et al.*, 2005; *Shepard and Helfenstein*, 2007; *Pommerol et al.*, 2013; *Souchon et al.*, 2011), and for investigations conducted for Mars using in situ (e.g. *Johnson et al.*, 1999, 2006a,b) and orbital measurements (e.g. *Erard et al.*, 1994; *Jehl et al.*, 2008; *Fernando et al.*, 2013a; *Shaw et al.*, 2013). In situ measurements provide information on the scattering behavior from rocks and soils at centimeter spatial scale and are limited to the rover path whereas orbital measurements provides those information from more extended areas integrating rocks and soils (hectometer to kilometer spatial scales) and can be obtained everywhere on the planet. The High Resolution Stereo Camera (HRSC) on-board Mars Express (MEx) has acquired multi-angular (up to five geometries per orbit) data of the Martian surface. *Jehl et al.* (2008) determined the regional variations of the photometric properties at the kilometer spatial scale across Gusev Crater and the south flank of Apollinaris Patera using several HRSC observations to enrich the diversity of available geometries. The photometric study was carried out without any atmospheric correction but ensuring that the atmospheric contribution was limited by selecting HRSC observations with mineral aerosol optical thickness lower than 0.9. Since 2006, the spectro-imager Compact Reconnaissance Imaging Spectrometer for Mars (CRISM) onboard Mars Reconnaissance Orbiter (MRO) provides multi-angular hyperspectral images (up to eleven geometries) giving the access to the surface material scattering behavior at the hectometer spatial scale. Recently, *Fernando et al.* (2013a) proposed an approach to estimate the surface photometric parameters by inverting the Hapke’s photometric model (*Hapke*, 1993, 2012a), including a robust and fast atmospheric correction called the Multi-angle Approach for Retrieval of the Surface Reflectance from CRISM Observations (MARS-ReCO) (*Ceamanos et al.*, 2013). The estimated photometric parameters provide information on the single scattering albedo and the main direction of the surface scattering (e.g. forward, backward) directly related to the physical state of the surface. Moreover, quantitative information on the surface roughness (roughness from millimeter to centimeter scales) are provided. In parallel, *Shaw et al.* (2013) derived maps of the single scattering albedo and the scattering asymmetric parameter at MER-Opportunity landing site at Meridiani Planum focused around the Victoria Crater, by using CRISM multi-angular observations, including an atmospheric correction.

In this paper, we apply the methodology developed by *Fernando et al.* (2013a) by including the mapping aspect to study the spatial variations of the scattering properties as a function of geological units in terms of surface photometric parameters. We try to link the surface photometric parameters in terms of physical properties by coupling with the orbital observations (e.g., CRISM/MRO spectral criteria, THERMAL EMISSION IMAGING SYSTEM (THEMIS) / Mars Odyssey thermal inertia values, High Resolution Imaging Science Experiment, (HiRISE)/MRO images and digital terrain model (DTM)) to provide information on the geological context. The present work focuses on the Mars Exploration Rover (MER) landing sites located at Gusev Crater and Meridiani Planum where orbital and in situ observations are available. This application is an example of what the methodology and the mapping can provide as information for the surface material physical characterization. The photometric results obtained from CRISM data are compared to the in situ observations (e.g., Panoramic camera (Pancam), Microscopic Imager (MI), Navigational camera (Navcam)), used as ground truth, to validate the photometric interpretations.

The article is organized as follows: (i) the methodology to obtain surface photometric parameters maps from the Hapke’s model is described in Section 2 and (ii) the analyses of these maps are presented and discussed by associating them with complementary orbital and in situ observations and with laboratory studies in Section 3. Then, we present (iii) the comparisons of the CRISM photometric results with a numerical model in Section 4.2 and (iv) the relations to the geological processes in Section 5.

2 Data sets and methods

2.1 CRISM targeted observations

The CRISM instrument on-board MRO is a visible and infrared hyperspectral imager (from 362 to 3920 nm at 6.55 nm/channel). The appropriate mode to estimate the surface spectro-photometric properties is the targeted mode given the Full Resolution Targeted observations (FRT) which provide the highest spatial resolution (15-20m/pixel). A targeted observation is a sequence of 11 hyperspectral images of a target area acquired at different emission angles thanks to the rotation of the detector at $\pm 70^\circ$. The solar incidence is almost constant during the spacecraft flyby over the target. The typical FRT sequence is composed of a central image ($\sim 10 \times 10$ km) at high spatial resolution (15-20m/pixel) and 10 off-nadir images with a x10 binning (150-200m/pixel) taken before and after the central image involving two azimuthal modes (*Murchie, S. et al.*, 2007).

2.2 Methodology

Fernando et al. (2013a) presented an approach to estimate the photometric parameters of the surface materials. The steps are summarized below.

2.2.1 Integration of multi-angular images

The eleven hyperspectral images of a FRT observation (reflectance and ancillary cubes) are spatially rearranged into a new data set called spectro-photometric curves (SPC) cube (*Ceamanos et al.*, 2013). In the present work, the integration of the multi-angle images has been improved. First, the central image taken at 15-20m/pixel is binned x10 to have the same spatial resolution as the 10 off-nadir images (150-200m/pixel). Second, all images are spatially combined to build the spectro-photometric curve of each spatial pixel by spatially associating each pixel of the central image (chosen as reference) with pixels from the 10 off-nadir images. We calculate the spatial nearest pixel by using the spatial coordinates of each image of the FRT observation and by taking into account the geometric deformation due to the detector gimbal (spatial resolution/cosine(emergence angle)). The association is performed when the overlapping between two pixels of two different images (central image and an off-nadir image) is at least 10%.

2.2.2 Correction for mineral aerosol contributions and estimation of the surface bidirectional reflectance

Ceamanos et al. (2013) proposed a technique referred to as MARS-ReCO to correct for mineral aerosols exclusively in order to estimate the surface bidirectional reflectance. For the present work, the surface bidirectional reflectance is estimated at 750 nm where the contribution from gas is negligible. The optical properties of mineral aerosol (particle size distribution and refractive index) and the mineral and water ice aerosol optical thickness ($AOT_{mineral}$ and AOT_{water}) of each observation is provided by Michael Wolff (*Wolff et al.* (2009), personal communication, 2011). The $AOT_{mineral}$ for each CRISM acquisition is used as an input of MARS-ReCO. MARS-ReCO is able to propagate the uncertainties on the surface bidirectional reflectance from the top-of-atmosphere (TOA) measurements. The different criteria for the use of the MARS-ReCO approach are presented in Sous-section 2.3.

2.2.3 Estimation of Hapke's photometric parameters

To analyze the surface bidirectional reflectance, the *Hapke* (1993, 2012b)'s model is used. This model depends on the geometric angles (incidence, emergence and phase angles) and on six parameters: the single scattering albedo, the particle phase function, the surface macroscopic roughness and the opposition effect parameters (Table 1). It is important to mention that CRISM is not observing Mars with phase angles less than 20°. Consequently the opposition effect parameter, B_0 and h , are underconstrained. The photometric parameters are estimated using a Bayesian inversion framework adapted for the inversion of the non-linear Hapke's model (*Fernando et al.*, 2013a,b). This technique is based on the concept of the state of information, characterized by a probability density function (PDF) (*Tarantola and Valette*, 1982). The prior information on model parameters (no information, defined as uniform PDF) combined with prior information on observations (a gaussian PDF) are fused to infer the solution by using the Bayes' theory. The final state of information (posterior PDF of each parameter) is numerically sampled using a Monte Carlo Markov Chain (*Mosegaard and Tarantola*, 1995) (see *Fernando et al.* (2013a,b) for more details) used to estimate the posterior PDF, the mean and the standard deviation of each Hapke photometric parameter.

2.3 Criteria for the selection of CRISM observations

Since September, 2010, the inbound segment in CRISM targeted mode is absent due to problems of the gimbal instrument (*Murchie*, 2012). In order to have the maximum number of geometries, only CRISM observations acquired before this date are selected.

The MARS-ReCO procedure is suitable for any CRISM observation within some constraints described below.

(1) Criterium on the mineral AOT and the water ice AOT. The accuracy of the determination of the surface reflectance, highly depends on the combination of a moderate mineral aerosol opacity ($AOT_{mineral} \leq 2$, (*Ceamanos et al.*, 2013)) and a low water ice aerosol opacity as the latter is not corrected by MARS-ReCO ($AOT_{water} \leq 0.2$, water ice content).

(2) Criterium on the geometries and the topography. The accuracy of the determination of the surface reflectance, highly depends on the geometries. The MARS-ReCO procedure is suitable for any CRISM multi-angular observation within some geometrical constraints: incidence angle $\theta_0 < 60^\circ$, phase angle range $\Delta g = g_{max} - g_{min} > 40^\circ$, outside the plan perpendicular to the principal plan ($\varphi_{inbound} = \varphi_{outbound} \sim 90^\circ$) (*Ceamanos et al.*, 2013). The local topography makes the photometric study more challenging when it is poorly known because it controls to a large extent the incidence,

Symbol	Definition	Physical significance	Geological significance
ω	Single scattering albedo	ratio of scattered light at the particle scale to extincted light	particle composition and size and microstructure
b	Asymmetry parameter ^a	anisotropy of the scattering ($b < 0.5$: broad / $b \geq 0.5$: narrow scattering lobe)	particle shape, composition and internal structure
c	Backscattering fraction ^a	main scattering direction ($c < 0.5$: forward / $c \geq 0.5$: backward scattering)	particle shape, composition and internal structure
B_0	Magnitude of the opposition effect	magnitude of the opposition effect peak ($g < 5^\circ$)	particle transparency ($B_0 = 0$: transparent particle, $B_0 = 1$: opaque particle)
h	Angular width of the opposition effect	angular half width of the opposition effect peak ($g < 5^\circ$)	surface porosity, particle size ($h = 0$: high porosity, $h = 1$: low porosity)
$\bar{\theta}$	Macroscopic roughness	mean slope angle inside a pixel expressed in degree	roughness from submillimetric-centimetric ranges

^aWe assume a two-term Henyey-Greenstein phase function (HG2)
 g : phase angle

Table 1: Summary of the Hapke photometric parameters and their physical and geological significance. All parameters are depending of the wavelength, set to 750 nm in the present work. Note that the parameters ω , b , c , B_0 and h vary from 0 to 1 and the parameter $\bar{\theta}$ varies from 0 to 45° .

emergence, and azimuth local angles. Besides, in the case of an oblique illumination (i.e., up to 70°), shadows decrease the signal/noise ratio. Only flat areas are selected.

The success of the MARS-ReCO procedure is evaluated by the percentage of corrected pixels. Observations with more than 50% of failed pixels after the MARS-ReCO procedure are rejected.

2.4 Evaluation on the accuracy of the surface photometric parameters estimates

After the MARS-ReCO correction, we can evaluate if the surface photometric curve (especially the diversity and number of available geometries) provides enough information to estimate accurate Hapke photometric parameter set by analyzing the shape of the a posteriori PDF. The criteria are summarized below.

(1) Non-uniformity criterion (k): A solution exists if the posterior PDF differs from the prior information (a uniform distribution). A statistical test is performed, leading to a non-uniformity criterion k (Fernando et al., 2013a). For $k \geq 0.5$, the posterior PDF is considered to be a non-uniform PDF meaning that a solution exists.

(2) Bimodality of the single scattering albedo PDF criterion: The presence of two possible solutions (e.g., bimodal distribution) is the consequence of the limitation of geometric diversity in the CRISM photometric curve to constrain the ω parameter (Fernando et al., 2013a,b), which is usually the best-constrained parameter in photometric modeling. Consequently, the other parameters should be underconstrained.

(3) Standard deviation (σ) criterion: It is used to characterize the dispersion around the mean value providing information on the accuracy of the solution. A solution is considered as well-constrained when $\sigma_\omega \leq 0.10$ for the ω parameter (which is the best constrained parameter in modeling), $\sigma_{b,c} \leq 0.20$ for the b and c parameters and $\sigma_{\bar{\theta}} \leq 5^\circ$ for the $\bar{\theta}$ parameter which are the less well-constrained parameters due the limited range of CRISM geometries.

The quality of the eleven images superimposing is crucial. Indeed, the ten off-nadir image footprints must ideally overlap the central image. However, due the surface topography uncertainty, the spacecraft position and attitude uncertainties and the gimbal jitter of the instrument, the superimposing is not always well-respected. Consequently, a worst quality of the image superimposing reduces the number of available angular configurations and the phase angle range. Only pixels with at least seven angular configurations are used for the estimation of surface photometric parameters. Tests using synthetic data set show that the sampling of photometric curve with less than seven geometries is not sufficient to accurately constrain the photometric parameters.

If all the criteria, presented before, are not respected that means that the diversity of geometries and the sampling of the surface bidirectional reflectance are not enough to constrain all the photometric parameters. The solution proposed by Pinet et al. (2005); Jehl et al. (2008); Fernando et al. (2013a) is to combine several observations acquired under varied illumination condition and assuming no surface changes to improve the diversity of geometries.

	ID	MER-Spirit		MER-Opportunity	
		FRT#C9FB	FRT#B6B5	FRT#334D	FRT#193AB
Time	Acquisition date	2008-09-21	2008-07-08	2006-11-30	2010-06-09
	L_s (deg.)	130.321	96	142.97	102.16
	θ_0 (deg.)	63	56	55	56
Geometry	$\varphi_{in} - \varphi_{out}$ (deg.)	$\simeq 55 - 131$	$\simeq 44 - 128$	$\simeq 64 - 117$	$\simeq 50 - 128$
	$g_{min} - g_{max}$ (deg.)	$\simeq 45 - 110$	$\simeq 40 - 106$	$\simeq 49 - 97$	$\simeq 39 - 105$
	Δg (deg.)	65	66	48	66
	$AOT_{mineral}$ (900 nm)	0.25 ± 0.03	0.35 ± 0.04	0.35 ± 0.04	0.31 ± 0.03
Atmosphere ¹	AOT_{water} (320 nm)	0.07 ± 0.03	0.14 ± 0.03	0.12 ± 0.03	0.13 ± 0.03
	uncorrected pixels (%)	9	33		13
MARS-ReCO	nb. of corrected pixels	868	1703		1492
	nb. of pixels with $k_b \geq 0.5$ (%)	100	99		100
	nb. of pixels with $k_c \geq 0.5$ (%)	100	99		89
	nb. of pixels with $k_{\bar{\theta}} \geq 0.5$ (%)	100	100		100
	nb. of pixels with $k_{\omega} \geq 0.5$ (%)	100	100		100
	Bayesian inversion	nb. of pixels with a bimodality	15	11	
	PDF for ω (%)				
	nb. of pixels with $\sigma_b \leq 0.20$ (%)	62	76		84
	nb. of pixels with $\sigma_c \leq 0.20$ (%)	55	25		28
	nb. of pixels with $\sigma_{\bar{\theta}} \leq 5^\circ$ (%)	83	56		52
	nb. of pixels with $\sigma_{\omega} \leq 0.1$ (%)	100	100		99

L_s : Solar longitude, θ_0 : incidence angle, $\varphi_{in} - \varphi_{out}$: CRISM inbound and outbound azimuthal angles, $g_{min} - g_{max}$: minimum and maximum of the phase angles, Δg : phase angle range, $AOT_{mineral}$: mineral aerosol optical thickness, AOT_{water} : water ice aerosol optical thickness, ω : single scattering albedo, b : asymmetric parameter, c : backscattering fraction, $\bar{\theta}$: macroscopic roughness, conf.: angular configurations, k : non-uniform criterion, σ : standard deviation, PDF: probability density function, ¹from Wolff’s estimates (Wolff *et al.*, 2009, personal communication)

Table 2: Selected CRISM FRT observations at the MER-Spirit’s and MER-Opportunity’s landing sites, respectively at Gusev Crater and Meridiani Planum with information on geometric, atmospheric conditions and statistic results relative to the MARS-ReCO procedure and to the Bayesian inversion of the Hapke model.

3 Results of CRISM photometric maps

3.1 MER-Spirit landing site at Gusev Crater

3.1.1 Selection of CRISM observations

Up to eleven FRT observations are available at the MER-Spirit landing site from the beginning of CRISM operations to September 2010. Among all, the observation FRT#C9FB shows the best satisfactory statistic results relative to the MARS-ReCO procedure and to the Bayesian inversion (satisfactory values of the non-uniform criterion (k), the standard deviation criterion (σ) and the bimodality of the single scattering albedo PDF criterion) (Table 2). The solutions estimated from the observation FRT#C9FB are used in the present study.

3.1.2 Geological context and study areas

Gusev Crater is an impact structure from the Noachian epoch, approximately 160 km in diameter and centered at 14.5° S/ 175° E (Kuzmin *et al.*, 2000). Proofs show a past fluvial and lacustrine activity from the 800-km long canyon called Ma’adim Vallis with sediment deposition that formed the hills (named Columbia Hills) (Kuzmin *et al.*, 2000; Cabrol *et al.*, 2003). However, some other authors recognized multiple eruptions of fluid basalts (Greeley *et al.*, 2005a) analogue to mare basalts (Greeley *et al.*, 1993). The region is also affected by seasonal aeolian processes. Hundreds of dark-toned, small sub-parallel streaks are observed. The tracks represent the removal of fine, bright-toned materials (more consistent with dust (Martinez-Alonso *et al.*, 2005)) from the basaltic underlying dark-toned materials by whirlwinds, called dust devils (Greeley *et al.*, 2003) and/or storms.

The context region of our work is presented in Figure 1: the selected CRISM FRT#C9FB observation is presented in Figure 1a and the geological map summarizing the different units and structures observed in the coupled HiRISE image (Figure 1b) is illustrated in Figure 1c. The HiRISE DTM image was used to calculate the mean slope at the meter per pixel (Figure 1d). Two units are discernible: the hills (Figure 1c in brown color), and the flat plain which is heavily cratered (referred to as Gusev cratered plain in following). Since the hills present high local slopes, it prohibits any treatment. In

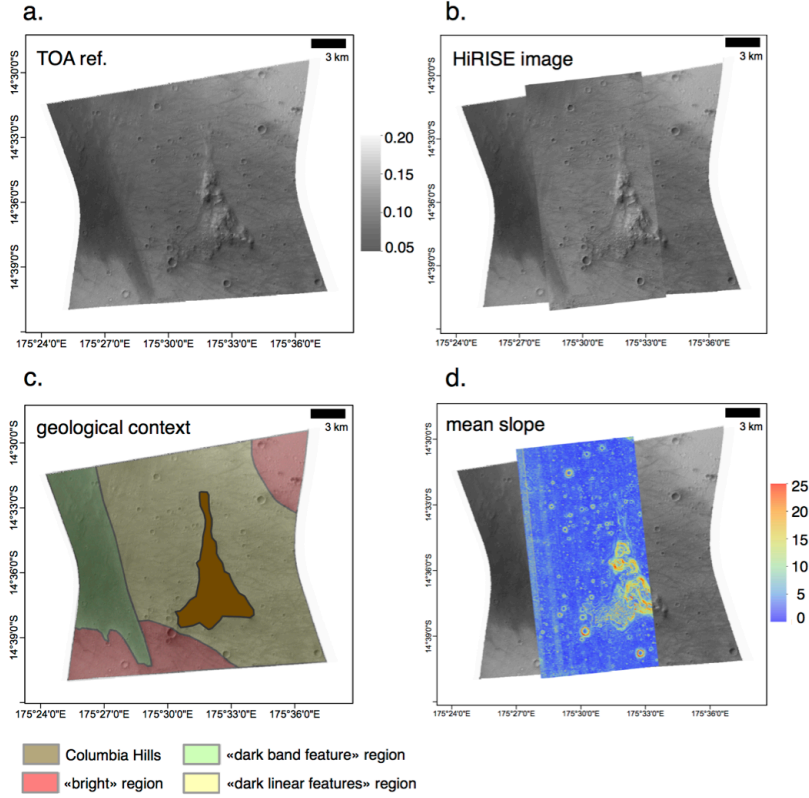


Figure 1: Geological context and studied area: a. CRISM TOA central images (FRT#C9FB) at 20m/pxl at 750 nm, b. CRISM TOA central images overlapped by the associated HiRISE image (PSP_010097_1655_RED), c. geological context map showing the different units and structures, CRISM TOA overlapped by the geological context map showing the different units and structures at 20m/pxl, d. CRISM TOA overlapped by the mean slope map at 1m derived from HiRISE Digital Terrain Model (DTM) (DTEEC_001513_1655_001777_1650_U01).

detail, three units are observed:

- (1) a dark-toned large band (NW-SE direction) associated with a dust storm track, referred to as “dark band feature” in following (Figure 1, in green color),
- (2) a region composed of numerous dark sub-parallel linear features (W-E direction) associated with dust devil tracks, referred to as “dark linear features” region in following (Figure 1, in yellow color),
- (3) a bright-toned region is observed in the NE part of the CRISM observations, referred to as “bright-toned” region in following (Figure 1, in red color).

The thermal inertia (TI) provides information on the bulk density, the particle size and the cohesion. From Thermal emission imaging system (THEMIS) onboard Mars Odyssey, the TI was estimated to $240 \pm 20 J.m^{-2}.s^{-0.5}.K^{-1}$ (spatial resolution of 100m/pixel) by *Milam et al.* (2003) who interpreted it as surface of medium-sized grain of sand.

In situ observations acquired by MER-Spirit rover, provide information on the surface physical and chemical properties from meter- to millimeter- scale of main geological units. *Arvidson et al.* (2006a) and *Arvidson et al.* (2008) provided an overview of key observations of soils and rocks. As presented before, we only focus on the Gusev plains. Along the traverse in the Gusev plains (Figure 2), images showed that the soil is composed of: (i) basaltic material excavated from lava flows by local impact (*Greeley et al.*, 2005a), (ii) a layer of dark coarse sands and granules (0.5 to a few mm in diameter) interpreted from Pancam to be rich-olivine basalts (*Bell et al.*, 2004), (iii) subangular lithic fragments interpreted to be ejecta deposits, which accompany the numerous craters, composed of clasts and rocks, and (iv) all coated with bright fine-grained material inferred to be dust (*Squyres et al.*, 2004a).

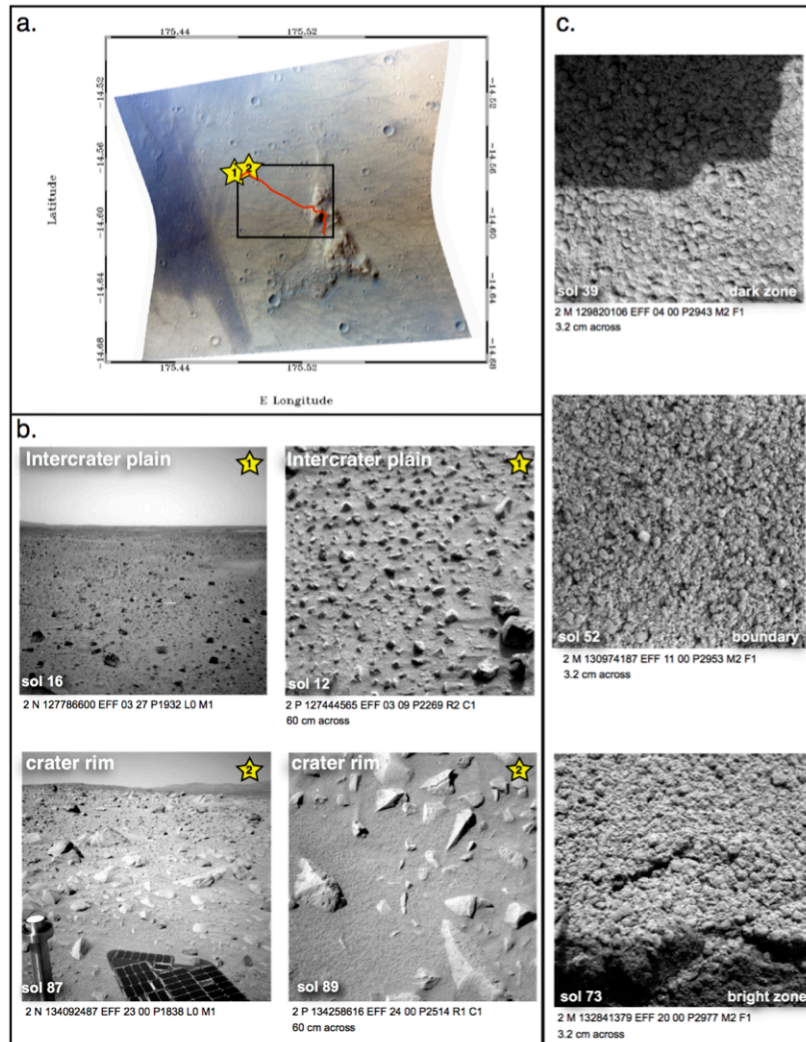


Figure 2: In situ observations from Navcam/MER (N), Pancam/MER (P) and MI/MER (M). (a) FRT#C9FB RGB image at $\sim 20\text{m/pxl}$ (credit: <http://crism-map.jhuapl.edu/>) with the rover path (in red color) and the locations of selected in situ images, (b) Navcam and Pancam images in the intercrater region (top) and near crater rim (bottom) and (c) MI images focused on inside a dust devil track (top), in the boundary (middle), and outside the dust devil track (bottom)

3.1.3 Surface material photometric parameters

3.1.3.1. The single scattering albedo parameter

Figure 3b represents the map of the single scattering albedo parameter (ω) values. Spatial variations of the ω parameter are observed at ~ 200 meters CRISM scale: (i) the “dark band feature” region (Figure 1, in green color) is correlated to the lowest ω values ($\omega < 0.60$, $\sigma \leq 0.10$), (ii) the “dark linear features” region (Figure 1, in yellow color) is correlated to intermediate ω values ($0.65 < \omega < 0.75$, $\sigma \leq 0.10$), (iii) the “bright-toned” region (Figure 1, in red color) is associated with the highest ω values ($\omega > 0.75$, $\sigma \leq 0.10$).

By comparing the ω values estimated from CRISM ($\omega_{CRISM} \simeq 0.65 - 0.75$) to those estimated from Pancam measurements at 753 nm located in our “dark-linear feature” geological unit for different geological units (rocks and soils) (Johnson *et al.*, 2006a) (Figure 4a), consistent ω values are obtained compared to the ω values obtained at Bonneville Rim site ($\omega_{Pancam} \simeq 0.66$), Landing Site and NW of Missoula areas ($\omega_{Pancam} > 0.7$).

Orbital observations showed that the Gusev Crater plain is composed of basalt, detected in the thermal infrared range by the Thermal Emission Spectrometer (TES) instrument on-board Mars Global Surveyor (MGS) (Milam *et al.*, 2003). Moreover, nanophase ferric-oxide-rich (npOx) bright dust is detected which covers the basaltic substrate detected by the Observatoire pour la Minéralogie, l’Eau, les Glaces et l’Activité (OMEGA) instrument on-board MEx over the MER-Spirit landing site (Lichtenberg *et al.*, 2007), confirmed by the in situ observations. To assess the surface dust, the nanophase ferric oxide spectral index is calculated from the CRISM data set (which is not corrected for mineral aerosol contribution) and mapped (Figure 5). Based on the presence of a broad near-infrared absorption between 0.75 and 1.0 μm due to the Fe^{3+} electronic transitions, the spectral ratio of the reflectance at wavelengths 1 μm and 0.8 μm is calculated (so called 1/0.8 μm slope) to estimate the nature of ferric oxide (Poulet *et al.*, 2007). Values close to 1 or greater are related to the high contamination of dust which masks the underlying materials. The dust index is sensitive to the mineral aerosol content in the atmosphere. However, the $AOT_{mineral}$ estimated for the FRT#C9FB is equal to 0.25 ± 0.03 (Table 2) that means that the atmosphere is less contaminated of mineral aerosols, and the highly structured spatial distribution of dust index in Figure 5, clearly shows surface signal.

By comparing the reflectance map at 750 nm (Figure 3a) and the ω map (Figure 3b) to the dust index map (Figure 5), three photometric regions are distinguishable. The region composed of “dark band feature” (Figure 1, in green color) is correlated to low or no dust signature (npOx $\simeq 0.90$) that means that the underlying basaltic surface may be visible. This region is correlated to the lowest ω values ($\omega_{CRISM} \simeq 0.60$, $\sigma \leq 0.10$). The “bright-toned” region in NE of CRISM observation (Figure 1, in red color) shows high dust signature (npOx close to 1) that means that dust cover the substrate, showing the highest ω values ($\omega_{CRISM} \simeq 0.80$, $\sigma \leq 0.10$). The region around and on the Columbia Hills (“dark linear features” region) (Figure 1, in yellow color) is correlated to intermediate dust index values (npOx $\simeq 0.95$) that mean dust partly contaminates the substrate and thus a complex signal from dust and basalt must be sensed (mixture). This area is correlated to intermediate ω values ($\omega_{CRISM} \simeq 0.65-0.75$, $\sigma \leq 0.10$).

In radiative transfer modeling, the single scattering albedo value is defined as a function of the composition, the particle size and the internal structure (Hapke, 1993, 2012a).

The single scattering albedo value decreases with the absorption coefficient: for a given particle size, a high absorption coefficient provides a low single scattering albedo values. At the studied wavelength (750 nm), similar optical constants (n , the refractive index and k , the absorption coefficient) are observed between a typical Martian dust ($n=1.50$, $k=0.001$, estimated from CRISM observation (Wolff *et al.*, 2009)) and a typical basalt ($n=1.52$, $k=0.0011$, estimated from laboratory measurements (Pollack *et al.*, 1973)). Consequently, the spatial variation of the parameter ω observed in Figure 3b cannot be explained by a composition variation.

The single scattering albedo value increases when the particle size value decreases. Because dust and basalt have very close optical constants, the highest ω values in the “bright-toned” region can be explained by the presence of finer particles compared to the region of “dark band feature”. Consistent analyses are observed by the rover. Two modes of particle size are observed in the Gusev plain: (i) a monolayer of basaltic coarse sands to very fine granules (between 500 and 2000 μm) Herkenhoff *et al.* (2004a); Herkenhoff, K. E., *et al.* (2006)) (Figure 2c, top) and (ii) on above, a bright dust deposit composed of particles from silt ($< 4 \mu m$ in diameter) (Lemmon *et al.*, 2004) to fine sand (mostly less than 150 μm) forming dust aggregates, Herkenhoff *et al.* (2004a); Sullivan *et al.* (2008); Vaughan *et al.* (2010) (Figure 2c, bottom). Intermediate ω values are observed in the region with numerous dust devil tracks with a width less than 100 meters which is lower than the CRISM spatial resolution ($\sim 200m/pixel$). Signal of some CRISM pixels may be a complex signal from dust and basalt. Indeed, along its traverse, the rover crossed albedo boundaries observed from Pancam images: the low-albedo dust devil tracks (0.20 ± 0.02) and the high-albedo dust deposit (0.30 ± 0.02) (Bell *et al.*, 2004). Greeley *et al.* (2004, 2005b) studied the high resolution MI images of the soils on the aeolian features: (i) inside the track, dust is removed and the underlying basalt is observed like coarse sand grains ($\simeq 1$ mm in diameter) but some dust particles remain which create an intimate mixture (Figure 2c, top), (ii) outside the tracks, a relatively thick dust cover may remain on the top of the

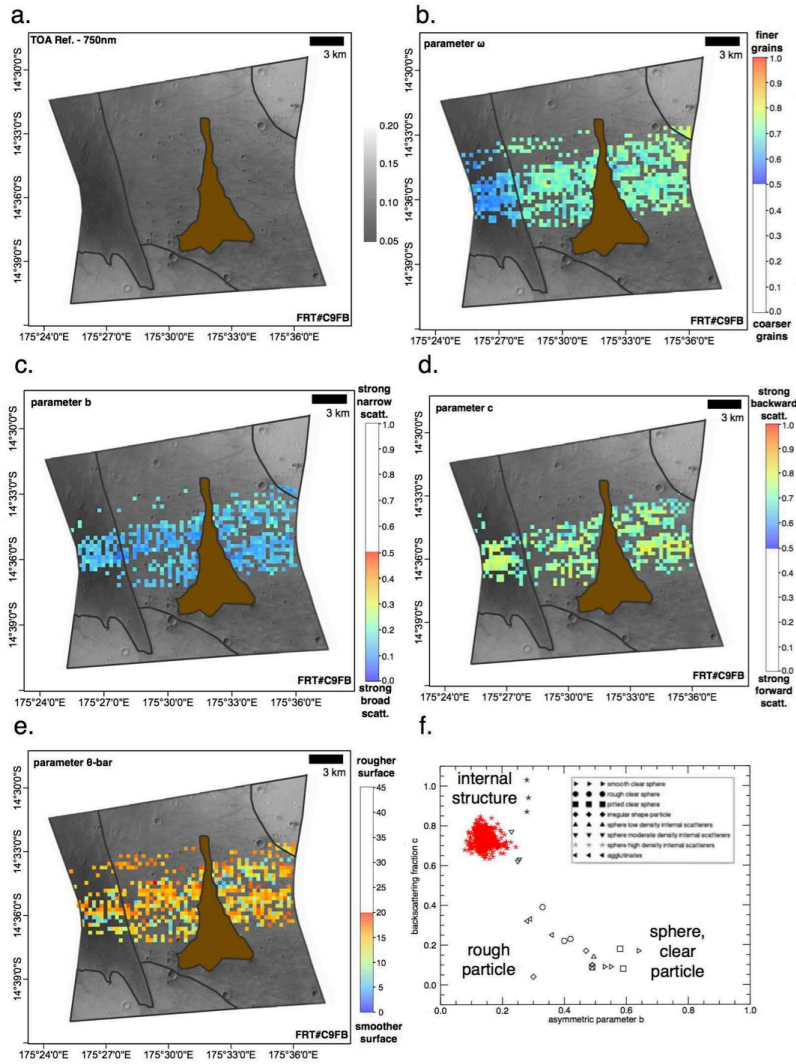


Figure 3: CRISM mapping (FRT#C9FB). a. TOA reflectance map in I/F unit at 20m/pixel at 750 nm. b. parameter ω map at 200m/pixel ($\sigma_\omega \leq 0.10$). c. parameter b map at 200m/pixel ($\sigma_b \leq 0.20$). d. parameter c map at 200m/pixel ($\sigma_c \leq 0.20$). e. parameter $\bar{\theta}$ map at 200m/pixel ($\sigma_{\bar{\theta}} \leq 5^\circ$). The colored pixels correspond to the value of the mean PDF. Only the middle part of the central image is covered with all additional geometric images (up to 11 images) that it is why the photometric results are obtained in this area. f. graph of the asymmetric parameter (b) versus backscattering fraction (c) estimated from FRT#C9FB plotted with experimental values on artificial particles from *McGuire and Hapke (1995)*.

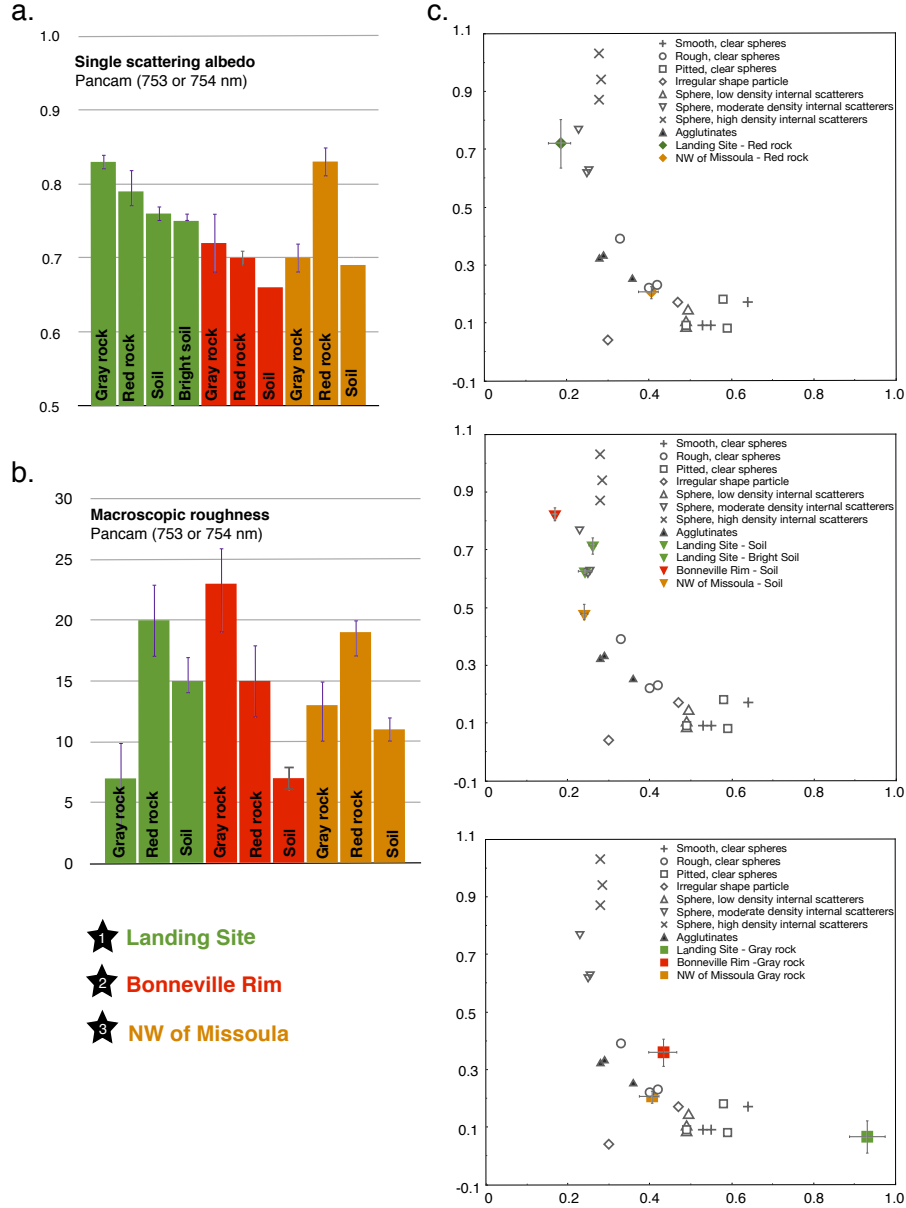


Figure 4: In situ photometric results from Pancam/MER: Mean and uncertainties of a. the single scattering albedo (ω), b. the macroscopic roughness ($\bar{\theta}$), c. the particle phase function parameters (b and c) overplot to the experimental b and c values pertaining to artificial particles measured by *McGuire and Hapke (1995)*. All photometric parameters are estimated at 753 or 754 nm for different geological units at Landing Site (Sol 013), Bonneville rim (Sol 087-088), and NW of Missoula (Sol 102-103) (*Johnson et al., 2006a*)

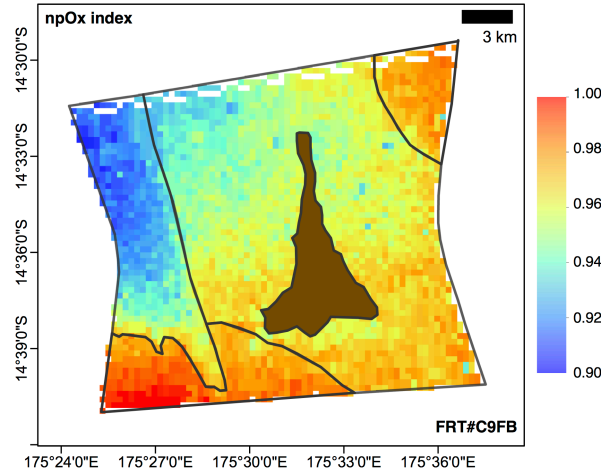


Figure 5: Composition map of nanophase ferric oxide spectral index (dust index) from FRT#C9FB: low or no dust areas have dust index less than 1 (blue tones) whereas dusty region have dust index greater or equal to 1 (red tones). The spatial resolution is 200m/pixel.

basalt in a stratified mixture (Figure 2c, bottom) and (iii) in the transition of outside and inside the tracks, a “pseudo” spatial mixture of both units may be detected.

The internal scatterers create also high scattering interactions inside the particle and increase the single scattering albedo values (*McGuire and Hapke, 1995*). The in situ observations from the MI instrument showed that dust particles are often observed as aggregates of individual unresolved finer particles (*Herkenhoff et al. (2004a); Sullivan et al. (2008); Vaughan et al. (2010)*), where the subparticles can act like internal scatterers. They also showed that the rocks on the Gusev floor are picritic basalts composed of mostly megacrystal olivines (abundance ranging up to 20-30 volume %) (*McSween et al., 2006*) which can act like internal scatterers. For basalt and dust, the ω values may be higher than their counterpart with no internal scatterers.

In conclusion, the spatial variation of ω parameter seems to be related at first order to the spatial variation of the particle size. This variation is caused by the dust removal (decrease in the ω values) and deposition (increase in the ω values) by aeolian processes by strong winds such as storms (such as the “dark band feature” region) or dust devils (such as “the dark linear feature” region) where silt-sized and sand-sized materials (dust and basalt) can be removed in suspension and by active saltation (*Greeley et al., 2006*). The ω values in the “dark linear feature” region result to a mixture (stratified, intimate, spatial) between basalt and dust (Figure 2c) tested by numerical modeling in subsection 4.2.

3.1.3.2. The particle phase function parameters

Figures 3c and 3d present the mean values of the a posteriori PDF for asymmetry parameter (b) and the backscattering fraction (c), respectively. The c parameter values show backscattering behavior (>0.5) and the parameter b values indicate broad scattering lobe (<0.5) for all pixels (Figures 3c, 3d and 3f). The local differences in the map are not significant in comparison to the error ($\sigma < 0.2$).

By comparing to the in situ photometric results, the CRISM results are consistent with b and c values estimated for Soil unit of different sites (*Johnson et al., 2006a*) (Figure 4c).

The particle phase function parameters are related to the grain shape (e.g., round, rough, irregular) and the grain internal scatterers (e.g., clear, fractures, minerals, pores) (*Hapke, 1993, 2012a*). To provide a physical meaning of the phase function parameters, experimental studies were conducted on well-characterized natural and artificial materials (*McGuire and Hapke, 1995; Shepard and Helfenstein, 2007; Souchon et al., 2011; Johnson et al., 2013*). *McGuire and Hapke (1995)* studied the scattering properties of different isolated artificial particles which had different structure types. Their study showed that smooth clear particles exhibit greater forward scattering (low values of c) and narrower scattering lobes (high values of b), whereas particles characterized by their roughness or internal scatterers exhibit greater backward scattering (high values of c) and broader scattering lobe (low values of b) (Figure 3f). By comparing to the *McGuire and Hapke (1995)*’s study, the scattering properties acquired from CRISM observation are closer to the scattering properties of artificial materials composed of particles with moderate density of internal scatterers (Figure 3c). Similarly, *Souchon et al. (2011)* measured, for a comprehensive set of geometries, the reflectance factor of natural granular surfaces composed of volcanic materials differing by their grain size, shapes, surface aspect, and mineralogy (including glass and minerals).

By comparing to the *Souchon et al. (2011)*'s works on natural volcanic samples, the scattering properties of "dark band" region where basalts are exposed (Figure 1, in green color) are closed to the scattering behavior of pyroclastics from Towada T6 (425-1000 μm) characterized by rounded grains with rough, hollowed and opaque surfaces with facets of phenocrysts and some isolated crystals. The results show that first the grains at the Gusev plain are rounded, like grains which are transported long distance by wind. Second, the results show that the grains are composed of a high density of internal scatterers suggesting the presence of a high density of crystals that means a high crystallization, and/or the presence of impurity (e.g., bubbles), properties totally different compared to a homogeneous grain like glass.

The MI images focused on a typical basaltic soil of coarse grains and cleaned of dust (Figure 2c, top) showed rounded and relatively spherical sands and granules as shown by *Greeley et al. (2006)* previously, consistent with the b and c values estimated from CRISM observation. Moreover, as presented previously, basalts are composed of mostly megacrystal olivines (abundance ranging up to 20-30 volume %) (*McSween et al., 2006*) which can act like internal scatterers (*McSween et al., 2006*), consistent with the high c value.

3.1.3.3. The surface macroscopic roughness parameter

Figure 3e represents the map of the macroscopic roughness parameter ($\bar{\theta}$) values. High $\bar{\theta}$ values ($\bar{\theta} \sim 15\text{-}20^\circ$, $\sigma \leq 5^\circ$) are observed, without significant spatial changes.

The macroscopic roughness parameter is related to the surface roughness created by the spatial organization of materials from millimeter- (silt and sand grains), centimeter (granule grains and rocks), up to decameter scales (*Hapke, 1993, 2012a*).

To explain the high $\bar{\theta}$ values, the mean slope is calculated from HiRISE DTM at scale of 1 meter per pixel (Figure 1c). In the cratered plains, we can identify 0.1-1 km diameter-size craters characterized by the highest mean slope (mean slope: $5 - 10^\circ$). The intercrater plain is characterized by the lowest mean slope (mean slope: $< 5^\circ$) (Figure 1c). By comparing the $\bar{\theta}$ parameter map to the mean slope, we note that the high $\bar{\theta}$ values are not correlated with a high mean slope that means that the macroscopic roughness parameter is not representative to the local topography at the meter-scale. The $\bar{\theta}$ parameter seems to be sensitive to the microscopic topography from millimeter- to centimeter- scale rather than larger scales, consistent with *Cord et al. (2003, 2005)*; *Helfenstein and Shepard (1999)*; *Shaw et al. (2013)*; *Shkuratov et al. (2005)*.

The HiRISE image provides information on the surface morphology and help for interpreting the surface macroscopic roughness values. The HiRISE image (Figure 1b) shows numerous craters which must be accompanied by numerous ejecta materials (clasts and rocks) from millimeter to several centimeter in size sprinkled the substrate (basaltic coarse sands and dust). The high population of spaced ejecta materials may create a high shadow hiding leading to a high macroscopic roughness values.

To validate the interpretation, the surface macroscopic roughness values obtained from CRISM are compared to those estimated from in situ photometric observations (Figure 4b) from Pancam (*Johnson et al., 2006a*) and to the in situ images (Figure 2b). The $\bar{\theta}$ values estimated from CRISM are more consistent with the Soil unit found at the Landing Site than the Soil unit at Bonneville Rim and NW Missoula. The main surface material change is the presence of a high proportion of clasts in soils of intercrater plains (Landing Site area) (Figure 2b), compared to the soils near to craters (Bonneville Rim and NW Missoula areas) (Figure 2b) where the Soil unit is devoid of clasts. Moreover, in contrary to Navcam and Pancam which operates from the ground and distinguishes rocks and soils (*Johnson et al., 2006a*), CRISM senses extended areas where rocks and soils are included. *Golombek et al. (2006)* estimated a rock abundance of about 5 to 35% of the surface materials according to the distance to the crater rim, that is consistent with the high macroscopic roughness values estimated from CRISM observation.

3.2 MER-Opportunity landing site at Meridiani Planum

3.2.1 Selection of CRISM observations

Up to seven FRT observations are available at MER-Opportunity landing site from the beginning of the CRISM operations to september 2010. Among all, the observations FRT#B6B5 and FRT#193AB show the best satisfactory statistic results relative to the MARS-ReCO procedure and the Bayesian inversion (satisfactory values of the non-uniform (k), the standard deviation (σ) criteria and the bimodality of the single scattering albedo PDF criterion) excepted for the parameter c of the observation FRT#B6B5 which shows a number of pixels with $\sigma_c \leq 0.20$ equal to 8%. To improve the geometric diversity of the FRT#B6B5, we combine the observations FRT#B6B5 and FRT#334D because they are superimposed, have complementary geometric acquisitions, and any surface change is observed. After the combination, the statistics of Bayesian inversion are improved, especially for the parameter c showing a number of pixels with $\sigma_c \leq 0.20$ equal to 25%. The solutions estimated from the combination of FRT#B6B5 and FRT#334D and from FRT#193AB are presented in the present work (Table 2).

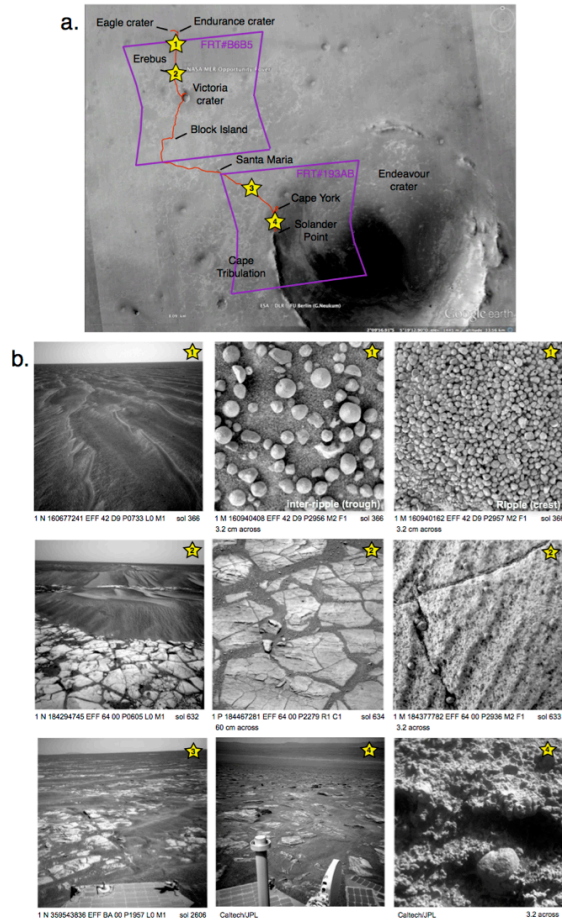


Figure 6: In situ observations from Navcam/MER (N), Pancam/MER (P) and MI/MER (M). (a) location of FRT#B6B5 (FRT#334D has the same footprint as FRT#B6B5) and FRT#193AB CRISM footprints (in purple color), the rover traverse (in red color) and the location of the selected in situ observations (star), (b) Navcam, Pancam and MI observations of the aeolian ripple region composed of hematitic concretions, basaltic sands and a small amount of dust (top line), Navcam, Pancam and MI observations of the aeolian ripple region with sulfate-rich outcrops at Erebus area (middle line) and Navcam and MI observations dark-toned sulfate-rich outcrops at Botany Bay at the west part of the Endeavour crater (bottom line).

3.2.2 Geological context and study areas

The MER-Opportunity landed in the Plains, Hematite-bearing (Ph) unit composed of patches light-toned sedimentary materials (etched terrain, ET2), overlain by a unconsolidated veneer of crystalline hematite bearing (plains mantle, Pm) detected by the TES instrument on-board MGS (*Christensen et al.*, 2000, 2001).

In July 2013, MER-Opportunity have crossed 38 km from the landing site near Eagle crater to Solander point (Figure 6a), the location where the rover was, during the writing of the present work. Two sites are presented in the present work: the surrounding of the Victoria crater (results from the combination of FRT#B6B5 and FRT#334D observations, called area 1), and the West side of Endeavour crater rim (results from the FRT#193AB observation, called area 2) (Figure 7a).

Victoria crater (area 1) The HiRISE image taken at the same local time as the FRT#B6B5 was used to make the geological context map. Four geological units are discernible:

- (1) Victoria crater (Figure 7c, brown color unit),
- (2) dark-toned materials mantle around the Victoria crater (Figure 7c, green color unit),
- (3) no or low population of bright-toned materials in the aeolian ripple troughs corresponding to the bedrock (etched terrain) associated with mid-toned materials in the ripple crests (Figure 7c, yellow color unit),
- (4) high population of bright-toned materials in the aeolian ripple troughs corresponding to the bedrock (etched terrain) associated with mid-toned materials in the ripple crests (Figure 7c, orange color unit).

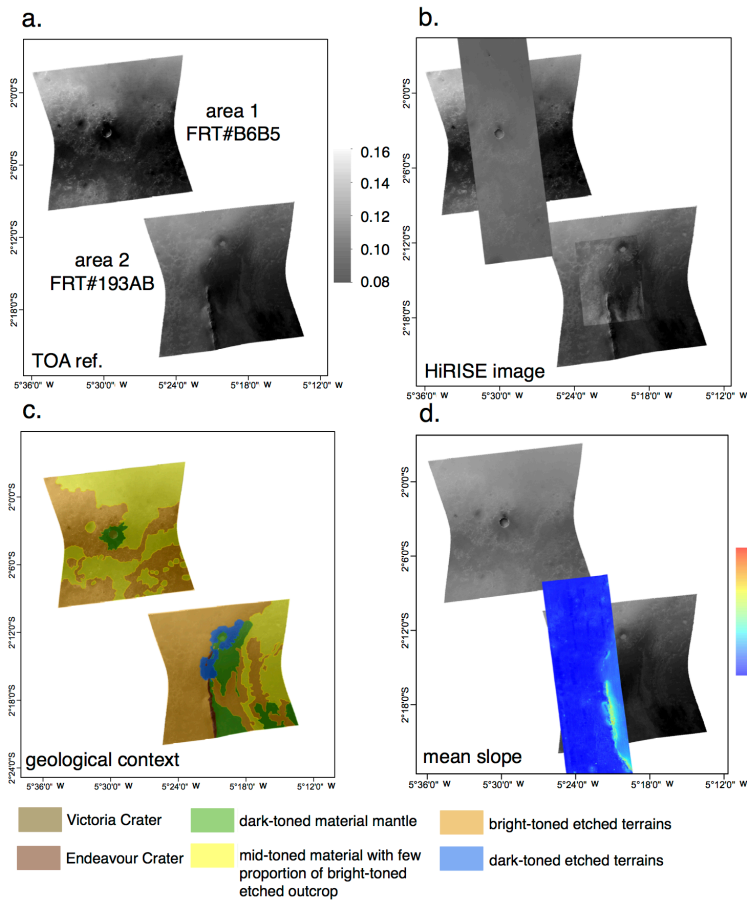


Figure 7: Geological context and studied area: a. CRISM TOA central images (FRT#B6B5 and FRT#193AB) at 20m/pxl at 750 nm, b. CRISM TOA central images overlapped by the associated HiRISE image (PSP_009141_1780_RED and ESP_032573_1775_RED), c. CRISM TOA overlapped by the geological context map showing the different units and structures, d. CRISM TOA overlapped by the mean slope map at 1m derived from HiRISE Digital Terrain Model (DTM) (DTEEC_018701_1775_018846_1775_U01).

Orbital reflectance spectra acquired by OMEGA on-board MEx, over the MER-Opportunity landing site are dominated by a basaltic sand cover mixed with crystalline hematite and small amount of dust (Arvidson *et al.*, 2006b). The abundant hydroxylated and hydrated sulfate minerals observed by the rover (Arvidson *et al.*, 2011; Squyres *et al.*, 2006) corresponding to the brighter terrains (Figure 7c, red and orange color units) identified in high resolution images (Figure 7b) have not been detected over the landing site at the OMEGA and CRISM spatial resolution scales. The region is characterized by low THEMIS TI values ($\sim 140 - 145 \text{ J.m}^{-2}.\text{K}^{-1}.\text{s}^{-1/2}$ (Arvidson *et al.*, 2011)) suggestive of the presence of fine-grained aeolian materials in the ripples whereas the region where bedrock is visible, the THEMIS TI values are slightly higher than ripples suggestive of the presence of indurated materials (Arvidson *et al.*, 2011).

Squyres *et al.* (2006) and Arvidson *et al.* (2011) provided an overview of key observations of soils and rocks observed by MER-Opportunity. Up to date, the in situ observations are available on Planetary Data System (<https://pds.jpl.nasa.gov>) up to sol 3240. Along the rover traverse (Figure 6a), the in situ observations showed that the Meridiani plain surfaces are covered by aeolian ripples (Figure 6b, top). The soil in the ripple troughs is dominated by rounded hematitic concretions, and fragments and their size is larger than those found in ripple crest soils (Figure 6) whereas the soil in the ripple crest is dominated by well-sorted hematitic concretions of a remarkable size distribution (Figure 6) (granule : 1-2 mm in diameter). Few millimeters beneath the lag of deposit, the interior is dominated by a mixture of basaltic sands, fragments of hematitic concretions and dust (Arvidson *et al.*, 2006a; Herkenhoff *et al.*, 2004b; Herkenhoff, K. E., *et al.*, 2006; Jerolmack *et al.*, 2006; Soderblom *et al.*, 2004; Weitz *et al.*, 2006; Squyres *et al.*, 2004b, 2006; Sullivan *et al.*, 2005) (Figure 6b, top line). From the Erebus Crater to the Endeavour crater (Figure 6a), bright-toned flat-lying bedrock outcrops (Figure 7c, in orange color units) are visible and are exposed in ripple troughs underlying the thin plain soil. The bedrocks are heavily desiccated and are characterized by fine laminations and have a high concentration of sulfur and contain abundant sulfate salts (Figure 6b, middle line) (Squyres *et al.*, 2004b). MI images showed that the outcrops bedrocks are composed of: (i) moderate rounded well-sorted sand grains (from 0.2 to 1 mm) forming mm-scale laminations, (ii) fine-grained and coarser precipitated cement crystals, (iii) cm-sized vugs that record the early diagenetic growth and subsequent dissolution of crystals, and (iv) 3- to 5-mm sized hematitic spherules embedded within the outcrops (Herkenhoff, K. E., *et al.*, 2006; Squyres *et al.*, 2004c).

West side of Endeavour crater rim (area 2) The HiRISE image taken at the same local time as the FRT#193AB was used to make the geological context map. Six geological units are discernible presented below.

(1) The discontinuous Endeavour rim (Cape York in the north and Cape Tribulation in the south) (Figure 7c, brown color unit) shows the highest THEMIS TI values ($>340 \text{ J.m}^{-2}.\text{K}^{-1}.\text{s}^{-1/2}$ (Chojnacki *et al.*, 2010)), suggestive of the presence of indurated materials (Arvidson *et al.*, 2011; Chojnacki *et al.*, 2010). The rim exposes basalt, iron and magnesium-rich smectite clay minerals (Wray *et al.*, 2009). The mean slope values derived from HiRISE DTM show high slopes greater than 15° (Figure 7d).

(2) The west part of the rim in the Meridiani plain is dominated by patches of bright-toned materials in the aeolian ripple troughs corresponding to the bedrock (etched terrain) associated with mid-toned materials in the ripple crests (Figure 7c, orange color unit). This area is characterized by higher THEMIS TI values ($\sim 155-180 \text{ J.m}^{-2}.\text{K}^{-1}.\text{s}^{-1/2}$ (Arvidson *et al.*, 2011)) than the etched terrains observed in the plains around the Victoria Crater. The mean slope values derived from HiRISE DTM show low slopes less than 5° (Figure 7d).

(3) The region around the rim called the Botany Bay area (Figure 7c, blue color unit), is composed of dark-toned outcrops (etched terrain), visible in the HiRISE image (Figure 7b) detected to be hydrated sulfate-rich bedrock (Wray *et al.*, 2009) from CRISM spectra.

(4) The Endeavour crater floor is characterized by a mantle of dark-toned materials (Figure 7c, green color unit), similar to the Ph unit.

(5) The crater floor is characterized by a low population of bright-toned materials corresponding to the bedrock similar to the etched unit associated with mid-toned materials in the ripple crests (Figure 7c, yellow color unit).

(6) The Endeavour crater floor is characterized by a high population of bright-toned materials corresponding to the bedrock similar to the etched unit associated with mid-toned materials in the ripple crests (Figure 7c, orange color unit).

The in situ observations showed bright-toned outcrops from the Erebus Crater to the Endeavour crater (Figure 6a) which are associated to sulfate-rich bedrocks exposed in ripple troughs. In the Botany Bay area, in situ observations showed platy polygonal fractured outcrops. The rocks are composed of layered features with rounded coarse-grained materials (sand-sized particles) embedded in a matrix and cement. A thin covering of soil settles the bedrocks but their quantity is not enough to form the wind-blown ripples. The desiccated features are filled with basaltic sands and hematitic concretions (report on <http://www.planetary.org/explore/space-topics/space-missions/mer-updates/2013/07-mer-update-opportunity-arrives-at-solander-suburb.html>).

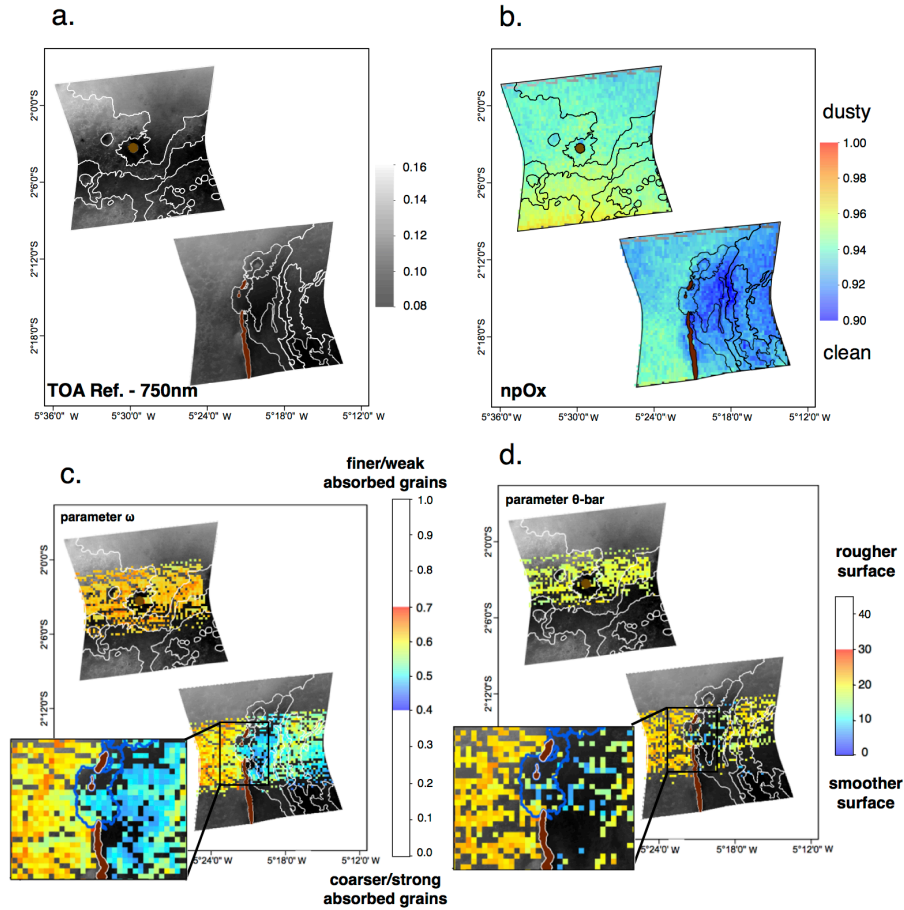


Figure 8: CRISM mapping of the combination of FRT#B6B5 - FRT#334D and FRT#193AB. a. TOA reflectance map in I/F unit at 20m/pixel at 750 nm. b. map of npOx spectral index (dust index) from FRT#B6B5 and from FRT#193AB at 200m/pixel. c. parameter ω map at 200m/pixel ($\sigma_\omega \leq 0.10$). d. parameter $\bar{\theta}$ map at 200/pixel ($\sigma_{\bar{\theta}} \leq 5^\circ$). The colored pixels correspond to the value of the mean PDF at about 200m/pixel. Only the middle part of the central image is covered with all additional geometric images (up to 22 images for area 1 and up to 11 images for area 2) that it is why the photometric results are obtained in this area.

3.2.3 Surface material photometric parameters

3.2.3.1. The single scattering albedo parameter

Figure 8c represents the map of the single scattering albedo values (ω). Spatial variations of the ω parameter are observed at 200m/pixel scale. In area 1, the regions mainly composed of dark-toned (Figure 7c, green color unit) and of mid-toned materials (Figure 7c, yellow color unit) are associated with the lowest ω values ($\omega_{CRISM} \leq 0.60$, $\sigma \leq 0.10$). The regions with a high proportion of bright-toned outcrops and accompanied with mid-toned materials (Figure 7c, orange color unit) are associated with the highest ω values ($\omega_{CRISM} \simeq 0.60 - 0.65$, $\sigma \leq 0.10$). In area 2, the crater floor composed of dark-toned material mantle (Figure 7c, green color unit) and the Botany Bay region (Figure 7c, blue color unit) are associated with the lowest ω values ($\omega_{CRISM} \simeq 0.40 - 0.50$, $\sigma \leq 0.10$). The bright-toned materials observed in the crater floor (Figure 7c, orange color unit) are associated with higher ω than surrounding but lower than the bright-toned outcrops observed in area 1 and in area 2 (Figure 7c, orange color unit) ($\omega_{CRISM} \simeq 0.60$, $\sigma \leq 0.10$).

From orbital observations, four components are observed: (i) hematitic concretions, (ii) basaltic sands, (iii) dust and (iv) sulfate, consistent with the in situ observations. The optical constants (n , and k) were found for basalt ($n=1.52$, $k=0.0011$) (Pollack et al., 1973), dust ($n=1.50$, $k=0.001$) (Wolff et al., 2009), hematite ($n=2.805$, $k=0.03478$) (Sokolik and Toon, 1999) and sulfate ($n=1.5$, $k=0.00001$) (Roush et al., 2007) at the studied wavelength (750 nm). Hematite mineral has the highest k coefficient (leading to lowest ω) and the sulfate mineral the lowest k coefficient (leading to highest ω). These are consistent with the CRISM ω results where the lowest ω values are observed in aeolian ripples without bright-toned outcrops, mainly composed of hematitic concretions (Figure 7c, yellow and green color unit). The highest ω

values are observed in regions associated with sulfate-rich bright-toned outcrops (Figure 7c, red and orange color units).

In situ images from Pancam and MI provide constraints on the particle size of each component, helpful for the ω values interpretation: (i) basalt characterized by fine-grained sands with a mean size around 50 to 150 μm (Herkenhoff, K. E., et al., 2006; Herkenhoff et al., 2004b; Weitz et al., 2006) (Figure 6b, top line), (ii) hematitic concretions dominated by a particle size around 1-2 mm (Herkenhoff, K. E., et al., 2006; Weitz et al., 2006; Herkenhoff et al., 2004b) (Figure 6b, top line), (iii) sulfate-rich bright-toned rocks composed of moderate rounded well-sorted sand grains (from 0.2 to 1 mm) forming mm-scale laminations, fine-grained and coarser cement crystals, cm-sized vugs, and 3- to 5-mm sized hematitic spherules embedded within the outcrops (Herkenhoff, K. E., et al., 2006; Squyres et al., 2004c) (Figure 6b, middle line), (iv) dust deposit of silt size ($<4 \mu\text{m}$ in diameter) (Lemmon et al., 2004) and (v) sulfate-rich dark-toned rocks composed of coarser grains (sand-sized) (report on <http://www.planetary.org/explore/space-topics/space-missions/mer-updates/2013/07-mer-update-opportunity-arrives-at-solander-suburb.html>) than the sulfate-rich bright-toned rocks (fine-sized). The coarse hematitic concretions (mm-sized) and the coarse grains in the sulfate-rich dark-toned rocks accentuates the decrease of ω values. The fine-grained size of the cement crystals in the bright-toned outcrops, of basalt, and the dust in the plains accentuates the increase of ω values, consistent with the CRISM ω estimates.

The internal scatterers create high scattering interactions inside the particle and increase the ω values (McGuire and Hapke, 1995). For the hematitic concretions, the MI images did not show macroscopic evidence of internal structures within the $\sim 100 \mu\text{m}$ resolution of the MI instrument (Herkenhoff et al., 2004b; McLennan et al., 2005; Herkenhoff et al., 2008). However, the emissivity measurements of the hematitic concretions from TES on-board MGS and Mini-TES on-board MER-Opportunity informed that the emissivity is dominated by emission along the crystallographic c axis explained by the lack of a 390 cm^{-1} feature in the hematite-rich spherule spectra (Lane et al., 2002; Glotch et al., 2004). To explain this observation, Glotch et al. (2006) from modeling and Golden et al. (2008) from experimental study suggested the presence of a high density of internal scatterers for the hematitic spherules (randomly oriented platy hematite crystal, concentric growth, or fibrous growth along the radial direction). For the sulfate-rich rocks, the MI images (Figure 6b) showed macroscopic evidence of heterogeneity in the sedimentary rocks with the presence of fine-grained and coarser cement crystals. For basalt, the MI resolution did not show evidence of internal structure within the $\sim 100 \mu\text{m}$ resolution of the MI instrument. However, basalt is generally composed of particles with high internal structures such as minerals or bubbles, like to the Gusev basaltic sands. For the three components (hematitic concretions, sulfate-rich rocks and basalt), the ω values may be higher than their counterpart with no internal scatterers, consistent with the CRISM ω estimates.

The single scattering albedo values estimated by CRISM are compared to those estimated from Pancam measurements (Johnson et al., 2006b) (Figure 9a). The goal is to understand and to provide a meaning of the mean scattering behavior measured by CRISM by coupling with the in situ observations. Indeed, the in situ instruments can distinguish rocks and soils whereas CRISM observes an extended area including rocks and soils (unit mixtures). Pancam measurements were taken at 753 nm for different geological units (rocks and soils): (i) the Outcrop unit refers to as the sulfate-rich bedrock, (ii) the Spherule soil unit refers to as unconsolidated materials of basaltic sands and of hematitic concretions, and (iii) the Ripple soil unit refers to as the ripple crest materials composed of basaltic sands and hematitic concretions and a small amount of dust (the population of hematitic concretions is greater than the Spherule soil unit) (Herkenhoff et al., 2004b; Johnson et al., 2006b; Herkenhoff, K. E., et al., 2006; Weitz et al., 2006). The Outcrop unit showed the highest ω values ($\omega_{\text{Pancam}} < 0.90$). For the Ripple soil and Spherule soil units, the lowest ω values are noticed ($\omega_{\text{Pancam}} < 0.60$). However, the Ripple soils unit showed lower ω values ($\omega_{\text{Pancam}} < 0.50$) than the Spherule soils ($\omega_{\text{Pancam}} < 0.60$). This discrepancy can be explained by the higher abundance of hematitic concretions in the ripple crests (accumulation during the wind transport) compared the ripple troughs and the soils (Herkenhoff et al., 2004b; Herkenhoff, K. E., et al., 2006; Weitz et al., 2006) (Figure 6b, top line). The comparison of the CRISM results to those estimated from in situ Pancam measurements is presented below.

(1) The regions mainly composed of mid-toned materials in areas 1 and 2 (Figure 7c, yellow color unit) show consistent values ($\omega_{\text{CRISM}} \leq 0.60$, $\sigma \leq 0.10$) with the Pancam estimates obtained for the Spherule soil and Ripple soil units ($\omega_{\text{Pancam}} < 0.60$).

(2) The regions with a high proportion of bright-toned outcrops and accompanied with mid-toned materials in areas 1 and 2 (Figure 7c, orange color unit) show lower values ($\omega_{\text{CRISM}} \simeq 0.60 - 0.70$, $\sigma \leq 0.10$) than the Pancam estimates ($\omega_{\text{Pancam}} \simeq 0.9$), that can be explained by the spatial resolution difference between Pancam and CRISM: Pancam distinguishes rock (e.g., Outcrop unit) and soil (e.g., Spherule soil and Ripple soil) whereas CRISM measures areas integrating different geological units. A mixture of Spherule soils or Ripple soil units characterized by lower ω values ($\omega_{\text{Pancam}} < 0.6$) with the Outcrop unit characterized by higher ω values ($\omega_{\text{Pancam}} < 0.9$), seems to slightly decrease the ω values consistent with the low ω values obtained from CRISM observation. In their experimental studies, Johnson et al. (2013) showed that the addition of 2-3 mm- sized spherules with thin hematite rims on an analog of the sulfate-rich sedimentary rocks composed of finer particles, decrease the ω values. The influence of mixtures in the scattering behavior between hematitic concretions and basalt and between hematitic concretions and sulfate are tested by numerical modeling in Subsection 4.2.

(3) The region at Botany Bay composed of dark-toned sulfate-rich outcrops (Figure 7c, blue color unit) shows lower values ($\omega_{CRISM} \simeq 0.45 - 0.50$, $\sigma \leq 0.10$) than those estimated for the Outcrops unit by Pancam ($0.77 < \omega_{Pancam} < 0.9$) that means there is a difference in the physical properties between both sulfate-rich outcrops. Coarser grains can explain the low ω values in the dark-toned outcrops regions confirmed by the in situ observations (report on <http://www.planetary.org/explore/space-topics/space-missions/mer-updates/2013/07-mer-update-opportunity-arrives-at-solander-suburb.html>).

(4) The regions composed of a dark-toned mantle in the Endeavour crater floor (Figure 6c, green color unit in area 2) show lower values ($\omega_{CRISM} \simeq 0.40 - 0.50$, $\sigma \leq 0.10$) than those estimated from the Spherule soil and Ripple soil units ($\omega_{Pancam} < 0.60$) and than those estimated at the region around Victoria Crater (Figure 6c, green color unit in area 1). Lower values are also observed compared to the region of aeolian ripples without sulfate-rich outcrops (Figure 7c, in yellow color unit). The npOx index value (Figure 8b) indicates that the surface is less and poorly contaminated by dust compared to all units in area 1. As observed at MER-Spirit landing site (Subsection 3.1.3), dust is characterized by high ω values ($\omega_{CRISM} \sim 0.80$). Consequently, their absence in the crater floor may decrease the mean ω values.

3.2.3.2. The particle phase function parameters

Figures 10a and 10c present the asymmetry parameter (b) and the backscattering fraction (c) respectively. At first order, the surface material is characterized by a broad backscattering behavior in both areas ($c > 0.5$ and $b < 0.5$). By comparing to the scattering parameters estimated from artificial particles by *McGuire and Hapke* (1995), the scattering properties estimated from CRISM observations are closer to the scattering behavior of artificial materials characterized by particles with moderate density of internal scatterers (Figure 10c). Moreover, we note that the c values are slightly higher in area 2 than in the area 1 (Figure 10b).

The particle phase function parameters estimated by CRISM are coupled to those estimated from Pancam measurements at 753 nm (*Johnson et al.*, 2006b) (Figure 9c) to understand the mean surface scattering behavior measurement by CRISM, presented below.

(1) The crater floor composed of dark-toned material mantle (Figure 7c, green color unit in area 2) shows the highest c values ($c_{CRISM} \sim 0.75 - 0.80$, $\sigma \leq 0.20$). Consistent values are observed with those estimated for Spherule soil and Ripple soil units (Figure 9c). The b and c values are consistent with the interpretation of the Mini-TES spectra which suggested that the hematitic concretions may be composed of concentric or radial interior structure. Moreover, the b and c values are consistent with the physical properties of typical basalt, composed of high internal structure such as basalt at MER-Spirit area (Subsection 3.1.3).

(2) The dark-toned sulfate-rich bedrocks observed at Botany Bay (Figure 7c, blue color unit in area 2) show the highest c values ($c_{CRISM} \sim 0.75 - 0.80$, $\sigma \leq 0.20$). We note a difference in the c values compared to aeolian ripples with sulfate-rich outcrops (Figure 7c orange and red color units) that suggests a difference in physical properties. The high c values can be explained by the presence of greater texture inside the rocks compared to the bright-toned outcrops. This is consistent with the in situ observations which showed that the dark-toned sulfate rocks are composed of coarser grains (sand-sized grains) embedded in a matrix and cement (report on <http://www.planetary.org/explore/space-topics/space-missions/mer-updates/2013/07-mer-update-opportunity-arrives-at-solander-suburb.html>).

(3) The regions mainly composed of mid-toned materials (Figure 7c, yellow color unit in areas 1 and 2), show intermediate c values ($c_{CRISM} \sim 0.60 - 0.75$, $\sigma \leq 0.20$). By comparing the c parameter values from CRISM to those estimated for the Spherule soil and Ripple soil units from Pancam, consistent values are found (Figure 9c). Lower c values are obtained, compared to the dark-toned mantle at Endeavour crater floor (Figure 7c, green color unit). This difference can be explained by the presence of small amount of dust in the aeolian ripples of dark-toned materials (the npOx index is close to 0.94, Figure 8b). *Johnson et al.* (2006c) showed a more forward scattering behavior for isolated dust particles, consistent with the scattering behavior of typical atmospheric dust particles as modeled by *Tomasko et al.* (1999) and *Lemmon et al.* (2004) over the Mars Pathfinder and MER landing sites. The mixture of dust with the unconsolidated materials of hematitic concretions and basalt can explain the decrease of c values.

(4) The regions with a high proportion of bright-toned outcrops and accompanied with mid-toned materials in area 1 (Figure 7c, orange color unit) show the lowest c values ($c_{CRISM} \sim 0.50 - 0.60$, $\sigma \leq 0.20$) and lower c values than the equivalent unit in area 2 ($c_{CRISM} \sim 0.70 - 0.75$, $\sigma \leq 0.20$). By comparing to the in situ photometric results from Pancam measurements (*Johnson et al.*, 2006b), higher c values are observed than those estimated from Pancam for Outcrop unit (Figure 9c). This difference can be explained by the difference of the spatial resolution where CRISM integrates the different geological units. A complex signal from different units (basalt, hematitic concretions, dust and sulfate-rich outcrops) is sensed by CRISM. In their experimental studies on Martian analogs, *Johnson et al.* (2013) showed that the addition of spherule $< 2 - 3$ mm in diameter with thin hematite rims on an analog of the spherule-bearing sulfate sedimentary rock composed of finer particles, increase the backscattering fraction. Indeed, as discussed before, this increase can be explained by the presence of radial or concentric growth inside the hematitic concretions which act

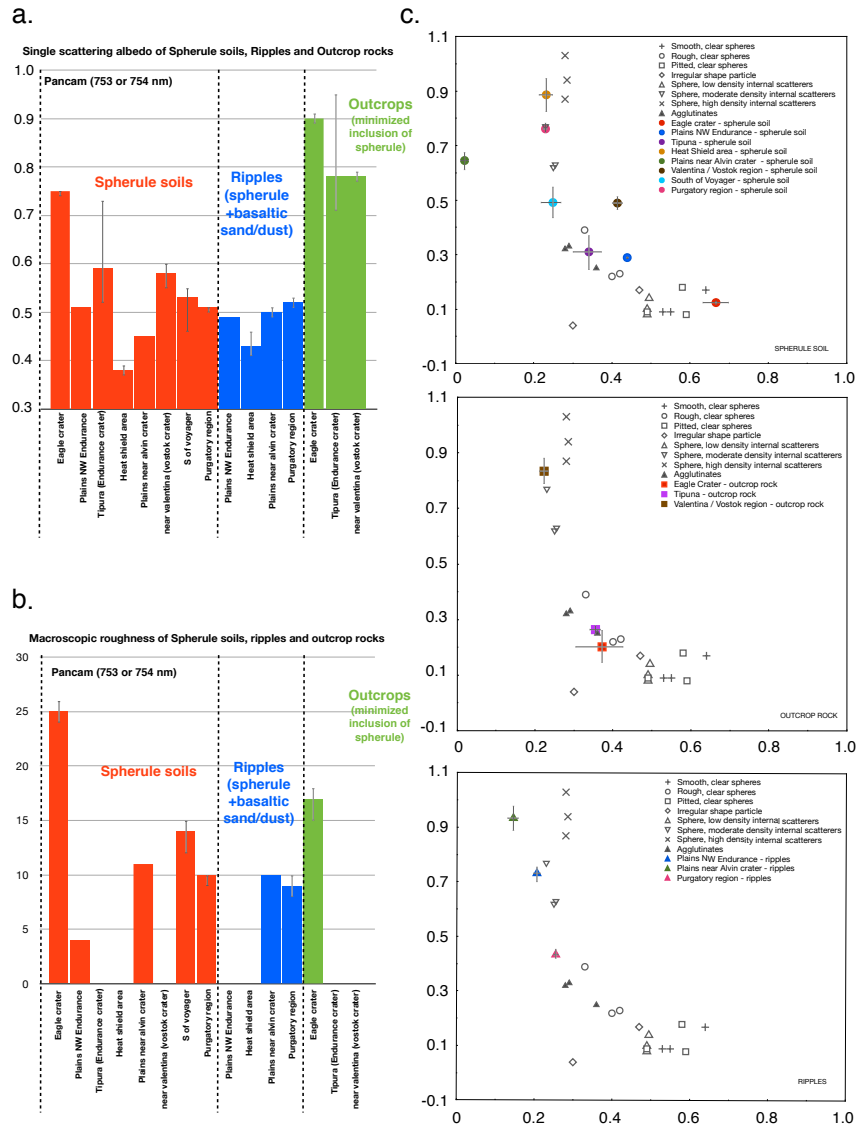


Figure 9: In situ photometric results from Pancam/MER: Mean and uncertainties of a. the single scattering albedo (ω), b. the macroscopic roughness (θ), c. the particle phase function parameters (b and c) overplot to the experimental b and c values pertaining to artificial particles measured by *McGuire and Hapke (1995)*. All photometric parameters are estimated at 753 or 754 nm for different geological units at different sites along the traverse (from Sol 11 to Sol 473) (*Johnson et al., 2006b*)

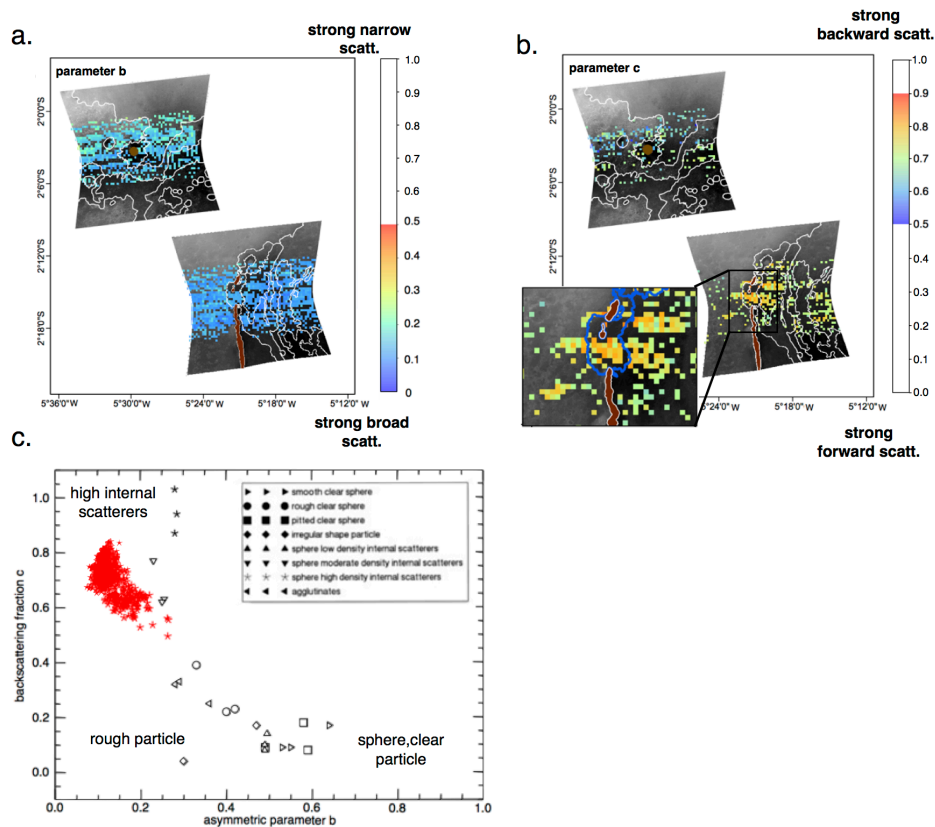


Figure 10: CRISM mapping of the combination of FRT#B6B5 - FRT#334D and FRT#193AB. a. parameter b map at 200m/pixel ($\sigma_b \leq 0.20$). b. parameter c map at 200m/pixel ($\sigma_c \leq 0.20$). The colored pixels correspond to the value of the mean PDF at about 200m/pixel. Only the middle part of the central image is covered with all additional geometric images (up to 22 images for area 1 and up to 11 images for area 2) that it is why the photometric results are obtained in this area. c. graph of the asymmetric parameter (b) versus backscattering fraction (c) estimated from FRT#193AB plotted with experimental values on artificial particles from *McGuire and Hapke (1995)*.

like internal scatterers (Subsection 3.2.3). The MI images (Figure 6b) of the sulfate-rich outcrops showed evidence of heterogeneity in the sedimentary rocks that creates high scattering, consistent with a high c value.

3.2.3.3. The surface macroscopic roughness parameter

Figure 8d represents the map of the surface macroscopic roughness parameter ($\bar{\theta}$) values related to the surface roughness. In general we observe high $\bar{\theta}$ values ($\sim 15-25^\circ$), higher than those estimated at Gusev plain. We note that: (i) the region with a high proportion of bright-toned outcrops and accompanied with mid-toned materials (Figure 7c, orange color unit) and the region mainly composed of mid-toned materials (Figure 7c, yellow color unit) are associated with the highest $\bar{\theta}$ values ($\bar{\theta}_{CRISM} \simeq 15-25^\circ$, $\sigma \leq 5^\circ$, Figure 8d), (ii) the Botany Bay region composed of dark-toned outcrops (Figure 7c blue color unit) and the dark-toned material mantle in the crater floor in area 2 (Figure 7c, green color unit) show the lowest $\bar{\theta}$ values ($\bar{\theta}_{CRISM} \simeq 5^\circ$, $\sigma \leq 5^\circ$, Figure 8d).

To explain the high $\bar{\theta}$ values, the mean slope is calculated from HiRISE DTM available in the area 2 at scale of 1 meter per pixel (Figure 7c). By comparing the $\bar{\theta}$ parameter map to the mean slope, the high $\bar{\theta}$ values are not correlated with a high mean slope that confirm again that the macroscopic roughness parameter is more sensitive to the microscopic topography from millimeter- to centimeter- scales also observed at the Gusev plains (Subsection 3.1.3) and consistent with the works from *Shaw et al.* (2013).

The macroscopic roughness values estimated by CRISM are coupled to those estimated from Pancam measurements at 753 nm (*Johnson et al.*, 2006b) (Figure 9b), to understand the mean surface scattering behavior estimated from CRISM observations, presented below.

(1) The regions mainly composed of mid-toned materials (Figure 7c, yellow color unit) show higher $\bar{\theta}$ values ($\bar{\theta}_{CRISM} \simeq 15-25^\circ$) than in situ photometric results (Figure 9b) for Spherule soil and Ripple soil units ($\bar{\theta} = 10-15^\circ$). In situ observations showed that most of Meridiani soils are composed of spaced millimeter-sized hematite spherules, above a sand-sized basalt deposit (Figure 6b). This particle disposition creates a high shadow hiding that explains the high $\bar{\theta}$ values. *Johnson et al.* 2013 showed in their experimental studies on Mars analog materials that the addition of spherules $< 2-3$ mm in diameter with thin hematite rims on an analog of the spherule-bearing sulfate sedimentary rock much finer particles (silt/sand size) caused the increase of the $\bar{\theta}$ values (from 7° to 26°), consistent with our observations. The discrepancy between Pancam and CRISM estimates can be explained by a difference of hematitic concretions density: a surface with well-spaced particles shows higher $\bar{\theta}$ values compared to a surface with closed particles.

(2) The regions with a high proportion of bright-toned outcrops and accompanied with mid-toned materials (Figure 7c, orange color unit) show consistent $\bar{\theta}$ values with the in situ photometric results (Figure 9b) estimated from Pancam measurements for Outcrop units ($\bar{\theta} = 15-20^\circ$). Again, the presence of small population of hematitic concretions on the sulfate-rich outcrops can create high shadow hidings that explains the high $\bar{\theta}$ values. Moreover, in situ observations showed that the sulfate-rich outcrops are highly textured with the presence of desiccation features and laminated surfaces that create a high local slope that can explain the high $\bar{\theta}$ values. A discrepancy is observed between aeolian ripples with sulfate-rich outcrops in the area 1 and those in the area 2 (Figure 1c, in orange color unit). This can be explained by higher exposure of sulfate outcrops in area 2 by the removal of superficial dust also observed in the npOx map (Figure 8b). The TI values estimated from THEMIS measurement are higher in the aeolian ripples in the area 2 than those observed in the area 1 (*Arvidson et al.*, 2011; *Chojnacki et al.*, 2010), consistent with the $\bar{\theta}$ values.

(3) The Botany Bay region composed of dark-toned sulfate rich outcrop (Figure 7c, blue color unit) shows the lowest $\bar{\theta}$ values ($\bar{\theta} \sim 5^\circ$, $\sigma \leq 5^\circ$, Figure 8d). The $\bar{\theta}$ values can be explained by smoother area with few density of hematitic concretions confirmed by in situ observations (report on <http://www.planetary.org/explore/space-topics/space-missions/mer-updates/2013/07-mer-update-opportunity-arrives-at-solander-suburb.html>).

(4) The dark-toned material mantle in the crater floor (Figure 7c, green color unit in area 2) shows the lowest $\bar{\theta}$ values ($\bar{\theta} \sim 5^\circ$, $\sigma \leq 5^\circ$, Figure 8d). Again, high density of hematitic concretions disposed nearby decreases the shadow hiding and thus can explain the low $\bar{\theta}$ values.

4 Modeling

4.1 Density of internal scatterers

The theoretical formulation of Hapke (eq. 6.47-6.50, *Hapke* (2012a)) is used to relate the single scattering albedo (ω) to the microscopic quantities. The microscopic quantities are: the complex indices of refraction (n and k) related to the particle composition, the path length (D) related to the particle size, the internal scattering coefficient (s), the density of internal scatterers (sD) related to the particle internal structure.

For the case of MER-Spirit landing site, the theoretical ω values of basalt and nanophase ferric oxide dust are calculated from the optical constants detailed in Table 3. First, the theoretical ω value is calculated for typical dust isolated

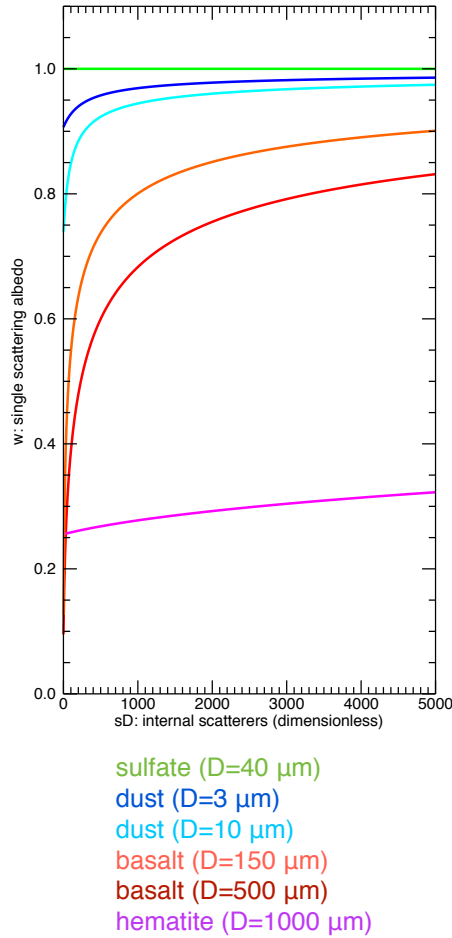


Figure 11: Graphe of the theoretical single scattering albedo (ω) as a function of the internal scattering coefficient (sD) for the typical particle size of basalt (500 μm , in red color), of dust (3 μm , in dark blue color and 10 μm , in light blue color), of hematite (1000 μm , in purple color) and of sulfate (40 μm , in green color).

atmospheric particles with a diameter 3 μm and no internal structure ($s=0$) (Lemmon *et al.*, 2004). We note that the theoretical ω value is around 0.9 (Figure 11) and is higher than the ω values estimated from CRISM observation ($\omega_{CRISM} \sim 0.80$). The low ω_{CRISM} value can be explained by dust with greater particle size. To have a low ω value, a coarse particle is needed. The theoretical ω value is calculated for coarser dust with a diameter 10 μm as a function of the density of internal scatterers (sD) (Figure 11). To have similar single scattering albedo values as to the CRISM estimates, internal scatterers must be included ($s = 3.8 \mu\text{m}^{-1}$ equivalent to $sD \sim 40$). This result is consistent with the in situ observations where dust is observed as aggregates of unresolved subparticles (Herkenhoff *et al.*, 2004a; Sullivan *et al.*, 2008; Vaughan *et al.*, 2010). Second, the theoretical ω value is calculated for typical basalt ($\simeq 500 \mu\text{m}$, Subsection 3.1.3, Herkenhoff *et al.* (2004a); Herkenhoff, K. E., *et al.* (2006)) for different values of s parameter. To have similar single scattering albedo values as to the CRISM estimates ($\omega_{CRISM} \sim 0.55$), $s = 0.68 \mu\text{m}^{-1}$ equivalent to $sD \sim 300$, must be used, consistent with the high CRISM c parameter values.

For the case of MER-Opportunity landing site, the theoretical ω values of hematite and sulfate are calculated from the optical constants and particle size detailed in Table 3. Because the MI spatial resolution is limited to $\sim 100 \mu\text{m}$ resolution, the component size of sulfate-rich outcrops is unknown. We decided to refer to the Johnson *et al.* (2013)'s experimental works. They selected a hematite-siderite spherule-bearing paleosol as an analog to the spherule-bearing sulfate-rich sedimentary rocks formed of a matrix soil of $< 45 \mu\text{m}$ particles. For a typical sulfate grain size ($\simeq 40 \mu\text{m}$) and the hematite grain size ($\simeq 1000 \mu\text{m}$), we note that the introduction of internal scatterers (sD) does not significantly change the ω value compared to basalt and dust (Figure 11). This is due to the fact that sulfate is very bright, and that hematite has a very large grain size, and their physical properties take precedence over the density of internal scatterers.

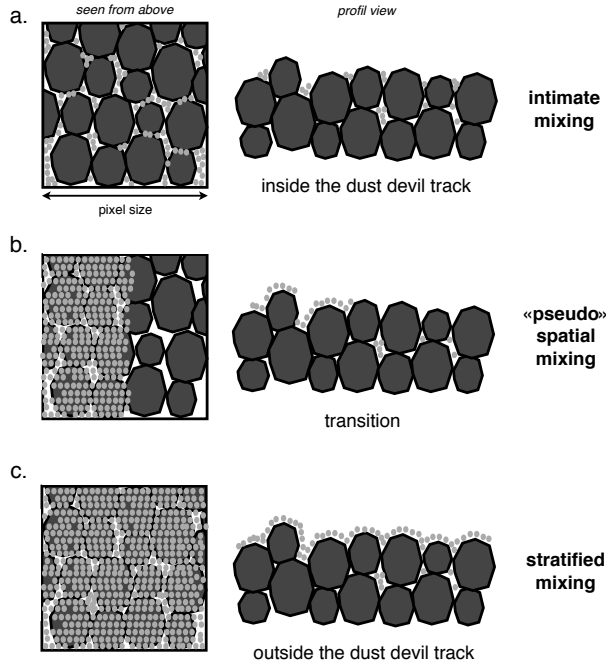


Figure 12: Schemes (seen from above and profil view) of different mixtures tested with the numerical model for the case of MER-Spirit area: (a) the intimate mixture observed inside a dust devil track, (b) “pseudo” spatial mixture in dust devil track transition, (c) the stratified mixture observed outside a dust devil track.

4.2 Mixtures

In natural environments, the planetary surfaces are composed of a mixture of different materials (e.g., dust deposit on basaltic unconsolidated materials observed at MER-Spirit landing sites, lag of hematite concretions on basaltic unconsolidated materials observed at MER-Opportunity landing sites). The influence of each component on the reflected radiation can be estimated through the use of numerical models that simulate the radiative transfer of different mixtures (basalt/dust, basalt/hematite and sulfate/hematite for example). We use here the *Pilorget et al. (2013)* model, which simulates light scattering in compact granular media using a Monte-Carlo approach. The physical and compositional properties can be specified at the grain scale allowing to simulate easily different kinds of mixtures (spatial, intimate and stratified). The radiative transfer is calculated by using a ray tracing approach between the grains and probabilistic physical parameters such as a single scattering albedo and a phase function at the grain scale. The single scattering albedo is calculated using *Hapke (1993, 2012a)* and thus is a function of the complex optical index of the material, the grain size and the potential inclusion of internal scatterers. A two-lobe Henyey-Greenstein phase function is also used in the model, consistently with the method described in previous sections. For more details about the model, please, refer to *Pilorget et al. (2013)*. The photons’ wavelength is 750 nm and their incidence angle is set at 45° . A porosity of 0.5 is assumed. The reflectance factor is computed in the $-80, +80^\circ$ emergence range. These results are then inverted by comparing and fitting the phase curves with the ones of homogeneous samples with various single scattering albedo and phase functions. Uncertainties are estimated to be within the ± 0.01 range for the parameter c and ± 0.02 for the parameter ω . The factors which control the mean scattering behavior of a medium for different kinds of mixtures (spatial, intimate and stratified) are studied in details in *Pilorget et al. (in preparation for Icarus)*.

In the MER-Spirit landing site at Gusev Crater, dust may cover the surface made of basalt grains or even fill the space pores between them in regions affected by dust devils (Figures 12a, 12b and 12c). We simulated both cases using the input parameter values summarized in Table 3.

Simulations show that when dust is situated within the space pores, only a small volume fraction is sufficient to hide the photometric response of basalt (Figures 12c, 15). Modeling results also show that a monolayer of dust ($10 \mu m$ thick) is sufficient to mask almost completely the photometric response of the underlying basalt and provide the best information on the dust scattering behavior (Figures 12c, 15). With 5% of dust in volume fraction, the parameter ω of the mixture is ~ 0.7 and the parameter c is ~ 0.69 , which is equivalent to 70% of surface area covered by a monolayer of dust (Figure 15).

These results show that in the Gusev crater area, the presence of dust (layer or in the space pores) drives the mean scattering behavior and masks the underlying material and the variability of scattering properties of materials. The dust

Site	Material	n	k	s (μm^{-1})	D (μm)	b	c
Spirit	dust	1.5 (Wolff <i>et al.</i> , 2009)	0.001 (Wolff <i>et al.</i> , 2009)	3.8 (Subsection 4.1)	10 (Lemmon <i>et al.</i> , 2004)	0.3	0.6^1 (Johnson <i>et al.</i> , 2006a)
	basalt	1.52 (Pollack <i>et al.</i> , 1973)	0.0011 (Pollack <i>et al.</i> , 1973)	0.68 (Subsection 4.1)	500 (Herkenhoff, K. E., <i>et al.</i> , 2006)	0.3	0.8 (Subsection 3.1.3)
Opportunity	hematite	2.805 (Sokolik and Toon, 1999)	0.03 (Sokolik and Toon, 1999)	0 (Subsection 4.1)	1000 (e.g. Herkenhoff <i>et al.</i> , 2008)	0.3	1.0 (Subsection 3.2.3)
	basalt	1.52 (Pollack <i>et al.</i> , 1973)	0.0011 (Pollack <i>et al.</i> , 1973)	0.68 (Subsection 4.1)	150 (e.g. Herkenhoff <i>et al.</i> , 2008)	0.3	0.8^3 (Subsection 3.1.3)
	sulfate	1.5 (Roush <i>et al.</i> , 2007)	10^{-5} (Roush <i>et al.</i> , 2007)	0 (Subsection 4.1)	40 (Johnson <i>et al.</i> , 2013)	0.3	0.2^1 (Johnson <i>et al.</i> , 2013)

n : refractive index, k : absorption coefficient, s : internal scattering coefficient, D : path length related to the particle size, b : the asymmetry parameter from the two-term Henyey Greenstein function, c : backscattering fraction from the two-term Henyey Greenstein function
¹ similar to the scattering properties of Bright soil unit of the Landing site obtained from Pancam (Johnson *et al.*, 2006a), corresponding to the most dustier area). The parameter b is constant for the both samples
² based on Johnson *et al.* (2013)'s experimental photometric results on an analog to the spherule-bearing sulfate sedimentary rocks observed at MER-Opportunity landing site
³ same b and c values estimated for basalt for the case of Gusev crater

Table 3: Physical parameters used for the mixture simulations.

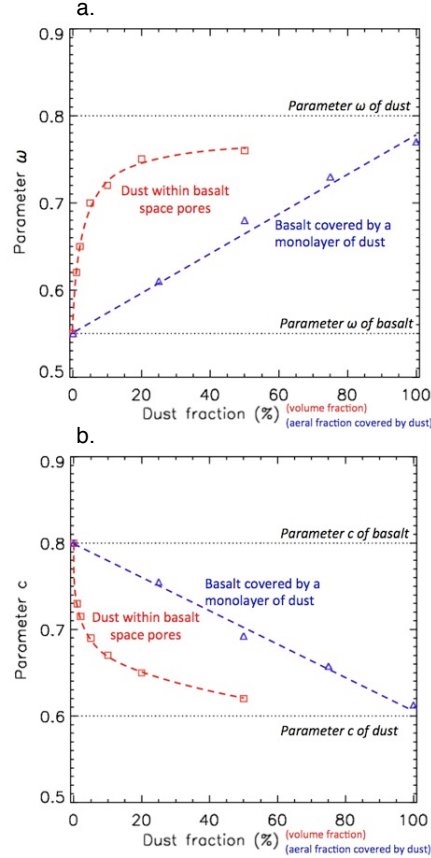


Figure 13: (Top) Evolution of the single scattering albedo (or parameter ω) and (Bottom) evolution of the backscattering fraction (or parameter c) when adding dust to a soil made of basalt. Both intimate (in red) and layered cases (in blue) are simulated. The grains sizes, optical parameters and phase functions used here are summarized in Table 3. For the intimate case, dust grains are set between the basalt grains (Figure 12a). For the layered case, dust grains are set as a monolayer on top of the basalt, such that a continuous areal fraction of the basalt is covered by the dust (Figures 12b and c). Since the porosity is set at 0.5, there are therefore always some voids between the dust grains. Results show that only a small fraction of dust is needed to hide the basalt photometric parameters (intimate case). When covering basalt by dust grains, the evolution of parameters ω and c tend to be linear as the areal fraction covered by dust increased, which is consistent with some kind of checkboard mixture. When dust covers 100% of the basalt, the influence of basalt is small but still exists since voids are still present between the dust grains. This behavior, however, highly depends on a combination of different factors such as the porosity (set here at 0.5), the geometric configuration and the grains parameters (optical index and phase function) and general trends about photometric behavior for layered mixtures should not be derived from these results.

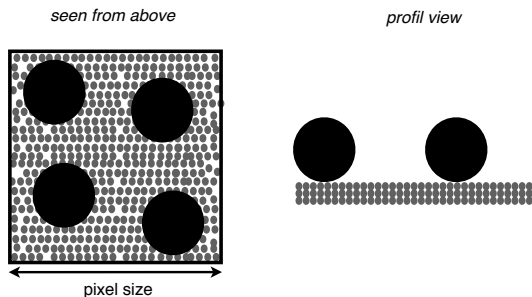


Figure 14: Schemes (seen from above and profil view) of mixtures tested with the numerical model for the case of MER-Opportunity area: hematitic concretions (coarse black grains) on basalt or on sulfate layers (finer grey grains).

devils are not sufficient to remove all dust (layer or in the space pores) from the surface materials and they remain between grains and in the porosity by the movement of grains. To assess to the scattering behavior of the underlying basalt, the area must be affected by stronger aeolian processes such as storms allowing the removal of all dust on the substrate such as the “dark band feature” region (subsection 3.1.3).

In the MER-Opportunity landing site at Meridiani Planum, hematitic concretions may cover the surface composed of basalt grains or composed of sulfate-rich outcrops (Figure 14). We simulated both cases using the input parameter values summarized in Table 3.

Results show that the addition of hematite to the basaltic surface or to the sulfate-rich surface decreases the surface brightness (Figures 15 and 16) and increases the c values where the scattering became more backward (Figures 15 and 16). Similar results were observed by *Johnson et al.* (2013) on their experimental studies where the addition of spherule $< 2 - 3$ mm in diameter with thin hematite rims on an analog of the spherule-bearing sulfate sedimentary rock composed of finer particles, decrease the single scattering albedo (from 0.97 to 0.84) and increase the backscattering fraction (from 0.16 to 0.419).

Regions with dark-toned mantle in the Endeavour crater floor (Figure 7, green color unit) are dominated by hematitic concretions on basaltic sands. By comparing the CRISM estimates ($\omega_{CRISM} = 0.40 - 0.50$) to the modeling results, the basaltic layer may be covered by an areal fraction of hematite from 10 to 30%. Regions with bright-toned outcrops (Figure 7, orange color unit) are dominated by sulfate-rich outcrops with hematitic concretions located in the ripple troughs and by hematitic concretions and basaltic sands in the ripple crests. By comparing the CRISM estimates ($\omega_{CRISM} = 0.60 - 0.70$) to the modeling results ($\omega_{model} = 0.70$), lower ω estimated from CRISM observations are observed. This discrepancy can be explained by the complex mixture of the surface. Indeed, the unit is composed of sulfate outcrop areas and ripple areas composed of a high fraction of hematitic concretions and basalt (Figure 6). The ripples are characterized by low ω values ($\omega_{CRISM} = 0.40 - 0.50$). The addition of hematitic concretions with the sulfate-rich outcrop unit can explain the low ω values, as observed previously.

5 Relations to the geological processes

In the previous section, we underlined the main photometric results and tried to provide a physical meaning in terms of particle size, shape, internal structure and surface roughness. The section focuses on the identification and the characterization of geological processes from the surface photometric results.

5.1 Gusev Crater

Volcanic resurfacing with the formation of the primary basaltic crust The phase function parameters and the single scattering albedo values show that the basaltic sands are particles with moderate density of internal scatterers. By comparing to the scattering properties of natural volcanic samples, these properties are related to materials characterized by rounded grains with rough, hollowed and opaque surfaces with facets of phenocrysts and some isolated crystals. This result indicates a high density of crystals in the basaltic sands (in contrary to volcanic glasses or olivine grains sands), consistent with the porphyric textures of the Gusev basaltic rocks composed of olivine megacrysts (abundance ranging up to 20-30 volume %) observed in the in situ observations (*McSween et al.*, 2006). This result means a relatively slow crystallization so that grains can grow. Moreover, the basalts have abundant vesicles and vugs, which can act like internal scatterers, consistent with the high c values suggesting eruption with high volatile contents (*McSween et al.*, 2006).

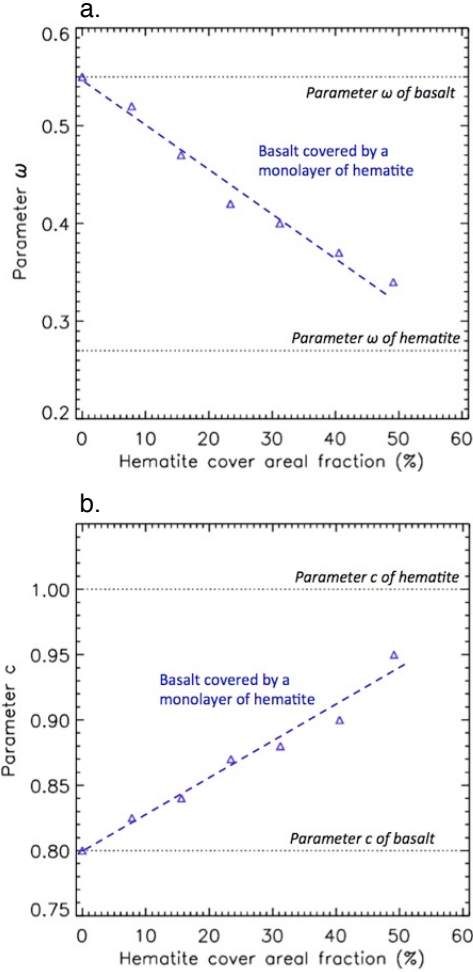


Figure 15: (Top) Evolution of the single scattering albedo (or parameter ω) and (Bottom) evolution of the backscattering fraction (parameter c) when adding hematite spheres (monolayer) on top of a soil made of basalt. The grains sizes, optical parameters and phase functions used here are summarized in Table 3. Hematite spheres are set randomly on top of the basalt grains (Figure 14). The areal fraction covered by hematite spheres represents the surface occupied by the spheres when looking at nadir. As the density of hematite spheres increases, the parameters ω and c evolve linearly (within the range of tested values). This behavior is however expected to change when the density is high enough because of geometric effects (only a fraction of the photons coming from the underlying basalt with specific directions can escape). As for the case presented in Figure 16, the behavior highly depends on a combination of different factors such as the porosity (set here at 0.5), the geometric configuration and the grains parameters (optical index and phase function) and general trends about photometric behavior for layered mixtures should not be derived from these results.

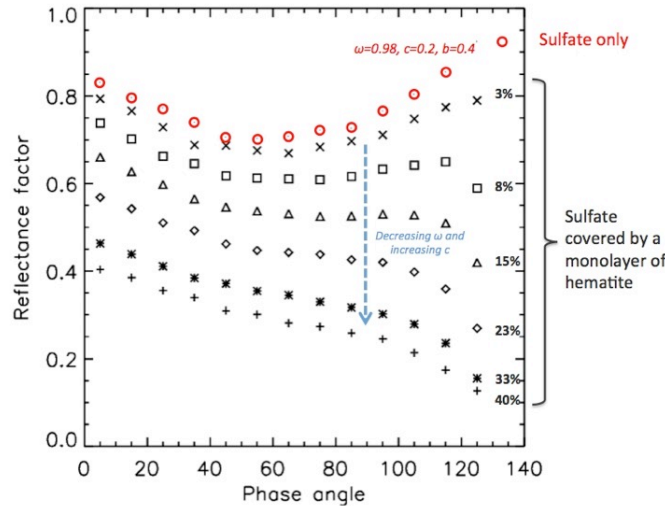


Figure 16: Evolution of the photometric curves when adding hematite spheres (monolayer) on top of a soil made of fine grained sulfates. The grains sizes, optical parameters and phase functions used here are summarized in Table 3. Hematite spheres are set randomly on top of the sulfate grains (Figure 14). The areal fraction covered by hematite spheres represents the surface occupied by the spheres when looking at nadir. Contrary to the case with basalt (Figure 15), geometric effects are very strong here. As the hematite density increases, the reflectance drops at high emergence (the photons that come from the underlying sulfates encounter the hematite spheres and are absorbed when escaping with high emergence angles). This effect is very strong when partially covering bright materials with some very absorbant one. No satisfactory fit could be obtained when trying to mimic this photometric behavior with the one of a homogeneous medium with parameters ω , b and c . Thus, only trends are indicated on the figure. Parameter ω could, however, be estimated to drop from 0.98 (no hematites) to about 0.7 (40% cover).

Fragmentation of the volcanic crust by bolide impact The high macroscopic roughness values suggest the presence of a high population of ejecta materials which accompany the numerous craters, consistent with the presence of spaced clasts and rocks along the rover traverse (*Squyres et al., 2004a; Grant et al., 2004, 2006; Golombek et al., 2006; Arvidson et al., 2006a; Ward et al., 2005*). This result reflects the fragmentation of the basaltic crust by local impacts and the emplacement of the ejecta materials. The high macroscopic roughness values reveal some difficulties for the rover landing and trafficability.

Aeolian processes with the reworking of the unconsolidated materials The single scattering albedo values indicate that dust seems to be a clumping of individual dust particles forming coarse aggregates where the subparticles acting like internal scatterers. This observation suggests that coarser than the individual dust particle with $3 \mu m$ in diameter can be found. *Sullivan et al. (2008); Vaughan et al. (2010)* identified the presence of dust aggregates ($\leq 150 \mu m$) observed in local areas in the MER-Spirit traverse, on the rover magnets and on solar panels. The aggregation of dust particles may be caused by electrostatic forces (*Greeley, 1979*). The aggregates are very fragile, porous, weakly dense makes them easier to be entrained by wind than individual dust particle ($\leq 4 \mu m$) or solid mafic grains of any large size ($\leq 300 \mu m$) (*Sullivan et al., 2008; Vaughan et al., 2010*). Then, these aggregates disaggregate back into their $\leq 3 \mu m$ particles by wind (*Sullivan et al., 2008*) due to their fragility and the violence of the passing of dust devils or strong winds contributing dust to the atmosphere. The removal of dust by aeolian processes (storms and dust devils) exposes the lower-albedo basalt characterized by coarse grains. *Thomas et al. (1984), Edgett and Malin (2000)* and *Greeley et al. (2005b)* suggested that the removal of a few micrometers thickness of dust from the surface could create a reflectance difference as seen in the ω parameter map. The phase function parameter values show that the basaltic sands are like rounded / spherical particles consistent with the in situ observations (*Greeley et al., 2006; McGlynn et al., 2011*). As discussed before, the Gusev basaltic crust were modified by bolide impacts. Consequently, the generated granular materials would be angular, such as typical lunar soils. The roundness of basaltic sands suggests that the materials were transported in long distance by wind and modified by post-aeolian processes (*McGlynn et al., 2011*). In the regions affected by dust devil events, intermediate single scattering albedo values suggest that dust remains on the surface materials. The MI observations showed that dust infiltrates among the monolayer of basaltic sands that suggests these sands are not currently experiencing saltation (*Greeley et al., 2006*). The radiative transfer modeling of an intimate mixture between dust and basalt indicates that

a small amount of dust can explain higher ω values and lower c values. Currently, only dust seems to be mobilized by aeolian processes (e.g., dust devils).

5.2 Meridiani Planum

The landing site is located in the Hematite-bearing (Ph) unit composed of patches light-toned sedimentary materials (etched terrain, ET2) overlain by a unconsolidated veneer of crystalline hematite bearing (plains mantle, Pm).

Sulfate-rich deposit The ET2 unit is composed of sulfate-rich outcrops identified in the aeolian ripple troughs and near the Endeavour crater rim. From HiRISE, the sulfate-rich outcrops in the ripple troughs are characterized by bright-toned materials whereas the sulfate-rich outcrops near the Endeavour crater are characterized by dark-toned materials. From photometric parameters, we note differences in the scattering behaviors between both etched terrains:

(1) The dark-toned etched terrains have lower ω than the bright-toned terrains ($\omega = 0.40 - 0.50$ for dark-toned etched terrains, $\omega = 0.60 - 0.65$ for bright-toned etched terrains). This result can be explained by the presence of coarser-grained particles in the dark-toned etched terrains.

(2) The dark-toned etched terrains have higher c than the bright-toned terrains ($c > 0.75$ for dark-toned etched terrains, $c < 0.75$ for bright-toned etched terrains). This result can be explained by the presence of greater texture inside the rocks of the dark-etched terrains.

(3) The dark-toned etched terrains have lower $\bar{\theta}$ than the bright-toned terrains ($\bar{\theta} = 5^\circ$ for dark-toned etched terrains, $\bar{\theta} = 15-25^\circ$ for bright-toned etched terrains). This result can be explained by the presence of platy sedimentary rocks, and/or less desiccated rocks in the dark-toned regions. The low macroscopic roughness values reveal that the dark-toned etched terrains are more convenient for the rover trafficability than the bright-toned terrains.

These differences suggest a different geological history during their formation, deposition and evolution. They can suggest different origins/natures of materials and different diagenesis mechanism and environments.

Lag of hematitic concretions The Pm unit is characterized by a mixture of hematitic concretions on basaltic sands. The single scattering albedo values and the phase function parameter values underlined the presence of coarse spherical hematitic concretions with moderate density of internal scatterers. *Golden et al.* (2010, 2008) synthesized hematite-rich spherules in laboratory along with hydronium jarosite and minor hydronium alunite from Fe-Al-Mg-S-Cl acid-sulfate solutions under hydrothermal conditions. They found similar mineralogical, chemical and crystallographic properties to the hematite-rich spherules observed by in situ observations at Meridiani Planum (*Golden et al.*, 2010, 2008). Their spherules exhibited a radial growth internal structures. The hematitic concretions are observed as lag deposits in the plains and as spherules embedded in the sulfate-rich sedimentary rocks *Arvidson et al.* (2011); *Grotzinger et al.* (2005); *Squyres et al.* (2004b, 2006); *Squyres, S. W. et al.* (2006); *McLennan et al.* (2005) suggested that the embedded hematitic concretions in the rock were produced by the erosion from the sulfate-rich sedimentary rocks and may be formed by postdepositional diagenesis within sandy sediments involving liquid water.

6 Conclusion

CRISM multi-angular observations allow to characterize the surface scattering behavior which depends on, the composition but also the material physical properties, such as the grain size, shape, internal structure, and the surface roughness and porosity. First an atmospheric correction (compensating mineral aerosol effects) by the MARS-ReCO algorithm is used to estimate more accurately the surface photometric curve taking into account the surface and mineral aerosol scattering anisotropy. Then the surface photometric curve is analyzed by inverting the Hapke's photometric model depending on six parameters: single scattering albedo, 2-term phase function, macroscopic roughness and 2-term opposition effects parameters, in a Bayesian framework. In the present work, surface photometric maps are created to observe the spatial variations of surface scattering properties at the CRISM spatial resolution ($\sim 200\text{m}/\text{pixel}$), as a function of geological units. The article is an application of the methodology on the Mars Exploration Rover (MER) landing sites located at Gusev Crater and Meridiani Planum. The orbital observations are used for interpreting the estimated Hapke photometric parameters in terms of physical properties providing useful information on the geological processes. The in situ observations are used as ground truth to validate the interpretations.

Varied scattering properties are observed inside a CRISM observation ($\sim 5 \times 10 \text{km}$) as a function of geological units suggesting variations of surface physical properties and surfaces are controlled by local geological processes rather than regional or global like volcanic resurfacing, fragmentation by impacts, aeolian processes, sulfates deposition and diagenesis.

We demonstrate that the macroscopic roughness parameter provides quantitative information on the surface roughness from millimeter- to centimeter-scales, useful for the selection of next rover landing sites due to engineering constraints on the landing and the trafficability.

Consistent results with the in situ observations are generally observed thus validating the approach and the use of photometry for the estimates of Martian surface physical properties. Some discrepancies can be noticed coming from a difference in the spatial scales. From the ground, the in situ instruments can distinguish rocks and soils (centimeter spatial scale), whereas CRISM observes extended areas (hectometric spatial scale) composed of different component of the surface (rocks and soils).

Future works will focus on the determination of surface photometric parameters of different geological terrains (sedimentary, volcanic terrains, impact craters, etc), in order to identify variabilities of scattering properties over Mars.

Acknowledgement . This work was supported by the French Space Agency CNES (Centre National d'Etudes Spatiales) and PNP (Programme National de Planétologie) from INSU (Institut National des Sciences de l'Univers). The authors would like to thank Michael Wolff for making his aerosol optical thickness values available for this study.

References

- Arvidson, R. E., et al. (2006a), Overview of the Spirit Mars Exploration Rover mission to Gusev Crater: Landing site to Backstay Rock in the Columbia Hills, *J. Geophys. Res.*, *111*, E02S01, doi:10.1029/2005JE002499.
- Arvidson, R. E., et al. (2006b), Nature and origin of the hematite-bearing plains of Terra Meridiani based on analyses of orbital and Mars Exploration rover data sets, *J. Geophys. Res.*, *111*, E12S08, doi:10.1029/2006JE002728.
- Arvidson, R. E., et al. (2008), Spirit Mars Rover Mission to the Columbia Hills, Gusev Crater: Mission overview and selected results from the Cumberland Ridge to Home Plate, *Journal of Geophysical Research: Planets*, *113*(E12), n/a–n/a, doi:10.1029/2008JE003183.
- Arvidson, R. E., et al. (2011), Opportunity Mars Rover mission: Overview and selected results from Purgatory ripple to traverses to Endeavour crater, *Journal of Geophysical Research: Planets*, *116*(E7), n/a–n/a, doi:10.1029/2010JE003746.
- Bell, J. F., et al. (2004), Pancam Multispectral imaging Results from the Spirit Rover at Gusev Crater, *Science*, *305*, no. 5685, 800–806, doi:10.1126/science.1100175.
- Cabrol, N. A., et al. (2003), Exploring Gusev Crater with Spirit: Review of science objectives and testable hypotheses, *Journal of Geophysical Research: Planets*, *108*(E12), n/a–n/a, doi:10.1029/2002JE002026.
- Ceamanos, X., S. Douté, J. Fernando, F. Schmidt, P. Pinet, and A. Lyapustin (2013), Surface reflectance of Mars observed by CRISM/MRO: 1. Multi-angle Approach for Retrieval of Surface Reflectance from CRISM Observations (MARS-ReCO), *J. Geophys. Res.*, *118*, doi:10.1029/2012JE004195.
- Chojnacki, M., J. Moerch, J. Wray, and D. Burr (2010), The stratigraphy, composition and thermophysical properties of Endeavour crater, Meridiani Planum, Mars, from orbital remote sensing, *Lunar Planet. Sci.*, XXXI, abstract 2175.
- Christensen, P. R., et al. (2000), Detection of crystalline hematite mineralization on Mars by the Thermal Emission Spectrometer: Evidence for near-surface water, *J. Geophys. Res.*, *115*, 9623–9642, doi:10.1029/1999JE001093.
- Christensen, P. R., R. V. Morris, M. D. Lane, J. L. Bandfield, and M. C. Malin (2001), Global mapping of Martian hematite mineral deposits: Remnants of water-driven processes on early Mars, *Journal of Geophysical Research: Planets*, *106*(E10), 23,873–23,885, doi:10.1029/2000JE001415.
- Cord, A. M., P. C. Pinet, Y. Daydou, and S. D. Chevrel (2003), Planetary regolith surface analogs: Optimized determination of Hapke parameters using multi-angular spectro-imaging laboratory data, *Icarus*, *165*, 414–427, doi:10.1016/S0019-1035(03)00204-5.
- Cord, A. M., P. C. Pinet, Y. Daydou, and S. D. Chevrel (2005), Experimental determination of the surface photometric contribution in the spectral reflectance deconvolution processes for a simulated martian crater-like regolithic target, *Icarus*, *175*, 78–91, doi:10.1016/j.icarus.2004.08.010.
- Edgett, K. S., and M. C. Malin (2000), Martian dust raising and surface albedo controls: Thin, dark (and sometimes bright) streaks and dust devils in MGS MOC high resolution images, *Lunar Planet. Sci.*, XXXI, abstract 1073.

- Erard, S., J. Mustard, S. Murchie, J. P. Bibring, P. Cerroni, and A. Coradini (1994), Martian aerosols: Near-infrared spectral properties and effects on the observation of the surface, *Icarus*, *111*, 317–337, doi:10.1006/icar.1994.1148.
- Fernando, J., F. Schmidt, X. Ceamanos, P. Pinet, S. Douté, and Y. Daydou (2013a), Surface reflectance of Mars observed by CRISM/MRO: 2. Zstimation of surface photometric properties in Gusev Crater and Meridiani Planum, *J. Geophys. Res.*, *118*, doi:10.1029/2012JE004194.
- Fernando, J., F. Schmidt, X. Ceamanos, P. Pinet, S. Douté, and Y. Daydou (2013b), Estimation of surface photometric parameters: Bayesian inversion on Hapke’s model, *EPSC*, *Vol. 8*, abstract 574.
- Glotch, T. D., R. V. Morris, P. R. Christensen, and T. G. Sharp (2004), Effect of precursor mineralogy on the thermal infrared emission spectra of hematite: Application to Martian hematite mineralization, *Journal of Geophysical Research: Planets*, *109*(E7), n/a–n/a, doi:10.1029/2003JE002224.
- Glotch, T. D., P. R. Christensen, and T. G. Sharp (2006), Fresnel modeling of hematite crystal surfaces and application to Martian hematite spherules, *Icarus*, *181*(2), 408 – 418, doi:http://dx.doi.org/10.1016/j.icarus.2005.11.020.
- Golden, D. C., D. W. Ming, R. V. Morris, and T. G. Graff (2008), Hydrothermal synthesis of hematite spherules and jarosite: Implications for diagenesis and hematite spherule formation in sulfate outcrops at Meridiani Planum, Mars, *American Mineralogist*, *93*, 1201–1214, doi:10.2138/am.2008.2737.
- Golden, D. C., D. W. Ming, and R. V. Morris (2010), Spherulitic growth of hematite under hydrothermal conditions: Insights into the growth mechanism of hematite spherules at Meridiani Planum, Mars, *Lunar Planet. Sci.*, abstract 2541.
- Golombek, M. P., et al. (2006), Geology of the Gusev cratered plains from the Spirit rover transverse, *J. Geophys. Res.*, *111*, E02S07, doi:10.1029/2005JE002503.
- Grant, J. A., et al. (2004), Surficial deposits at Gusev Crater along Spirit rover traverses, *Science*, *305*, no. 5685, doi:10.1126/science.1099849.
- Grant, J. A., S. A. Wilson, M. Ruff, S. W. Golombek, and D. Koestler (2006), Distribution of rocks on the Gusev plains and on Husband Hill, Mars, *J. Geophys. Res.*, *33*, L16,202, doi:10.1029/2006GL026964.
- Greeley, R. (1979), Silt-clay aggregates on Mars, *Journal of Geophysical Research: Solid Earth*, *84*(B11), 6248–6254, doi:10.1029/JB084iB11p06248.
- Greeley, R., et al. (1993), Galileo imaging observations of Lunar maria and related deposits, *Journal of Geophysical Research: Planets*, *98*(E9), 17,183–17,205, doi:10.1029/93JE01000.
- Greeley, R., R. O. Kuzmin, S. C. R. Rafkin, T. I. Michaels, and R. Haberle (2003), Wind-related features in Gusev Crater, Mars, *J. Geophys. Res.*, *108*, E128,077, doi:10.1029/2002JE002006.
- Greeley, R., et al. (2004), Wind-related processes detected by the Spirit rover at Gusev Crater, Mars, *Science*, *305*, no. 5685, doi:10.1126/science.1100108.
- Greeley, R., B. H. Foing, H. Y. M. Jr., G. Neukum, M. v. K. P. Pinet, S. C. Werner, D. A. Williams, and T. E. Zegers (2005a), Fluid lava flows in Gusev Crater, Mars, *J. Geophys. Res.*, *110*, E05,008, doi:10.1029/2005JE002401.
- Greeley, R., et al. (2005b), Martian variable features: New insight from the Mars Express orbiter and the Mars Exploration Rover Spirit, *J. Geophys. Res.*, *110*, E06,002, doi:10.1029/2005JE002403.
- Greeley, R., et al. (2006), Gusev Crater: Wind-related features and processes observed by the Mars Exploration Rover Spirit, *J. Geophys. Res.*, *111*, E02S09, doi:10.1029/2005JE002491.
- Grotzinger, J., et al. (2005), Stratigraphy and sedimentology of a dry to wet eolian depositional system, burns formation, Meridiani Planum, Mars, *Earth and Planetary Science Letters*, *240*(1), 11 – 72, doi:http://dx.doi.org/10.1016/j.epsl.2005.09.039, <ce:title>Sedimentary Geology at Meridiani Planum, Mars</ce:title>.
- Hapke, B. (1993), *Theory of Reflectance and Emittance Spectroscopy*, Cambridge Univ. Press.
- Hapke, B. (2012a), *Theory of Reflectance and Emittance Spectroscopy*, Cambridge Univ. Press.

- Hapke, B. (2012b), Bidirectional reflectance spectroscopy 7 the single particle phase function hocky stick relation, *Icarus*, *221*, 1079–1083, doi:10.1016/j.icarus.2012.10.022.
- Helfenstein, P., and M. K. Shepard (1999), Submillimeter-scale topography of the Lunar regolith, *Icarus*, *141*(1), 107 – 131, doi:http://dx.doi.org/10.1006/icar.1999.6160.
- Herkenhoff, K. E., et al. (2004a), Textures of the soils and rocks at Gusev Crater from Spirit’s Microscopic Imager, *Science*, *305*, 5685, doi:10.1126/science.3050824.
- Herkenhoff, K. E., et al. (2004b), Evidence from Opportunity’s Microscopic Imager for water on Meridiani Planum, *Science*, *306*(5702), 1727–1730, doi:10.1126/science.1105286.
- Herkenhoff, K. E., et al. (2008), Surface processes recorded by rocks and soils on Meridiani Planum, Mars: Microscopic Imager observations during Opportunity’s first three extended missions, *J. Geophys. Res.*, *113*, E12S32, doi:10.1029/2008JE003100.
- Herkenhoff, K. E., et al. (2006), Overview of the Microscopic Imager investigation during Spirit’s first 450 sols in Gusev Crater, *J. Geophys. Res.*, *111*, E02S04, doi:10.1029/2005JE002574.
- Jehl, A., et al. (2008), Gusev photometric variability as seen from orbit by HRSC/Mars-Express, *Icarus*, *197*, 403–428, doi:10.1016/j.icarus.2008.05.022.
- Jerolmack, D. J., D. Mohrig, J. P. Grotzinger, D. A. Fike, and W. A. Watters (2006), Spatial grain size sorting in eolian ripples and estimation of wind conditions on planetary surfaces: Application to Meridiani Planum, Mars, *J. Geophys. Res.*, *111*, E12S02, doi:10.1029/2005JE002544.
- Johnson, J. R., et al. (1999), Preliminary results on photometric properties of materials at the Sagan Memorial Station, Mars, *J. Geophys. Res.*, *104*, 8809–8830, doi:doi:10.1029/98JE02247.
- Johnson, J. R., et al. (2006a), Spectrophotometric properties of materials observed by Pancam on the Mars Exploration Rovers: 1. Spirit, *J. Geophys. Res.*, *111*, E02S14, doi:10.1029/2005JE002494.
- Johnson, J. R., et al. (2006b), Spectrophotometric properties of materials observed by Pancam on the Mars Exploration Rovers: 2. Opportunity, *J. Geophys. Res.*, *111*, E12S16, doi:10.1029/2006JE002762.
- Johnson, J. R., et al. (2006c), Radiative transfer modeling of dust-coated pancam calibration target materials: Laboratory visible/near-infrared spectrogoniometry, *J. Geophys. Res.*, *111*, E12S07, doi:10.1029/2005JE002658.
- Johnson, J. R., M. K. Shepard, R. Grundy, D. A. Paige, and E. Foote (2013), Spectrometry and modeling of Martian and Lunar analog samples and Apollo soils, *Icarus*, *223*, 383–406, doi:10.1016/j.icarus.2012.12.004.
- Kuzmin, R., R. Greeley, R. Landheim, N. Cabrol, and J. Farmer (2000), Geologic map of the MTM-15182 and MTM-15187 quadrangles, Gusev crater - Ma’adim Vallis region, *Mars. Geologic Investigative Series, U.S. Geological Survey, Reston, VA*.
- Lane, M. D., R. V. Morris, S. A. Mertzman, and P. R. Christensen (2002), Evidence for platy hematite grains in Sinus Meridiani, Mars, *Journal of Geophysical Research: Planets*, *107*(E12), 9–1–9–15, doi:10.1029/2001JE001832.
- Lemmon, M. T., et al. (2004), Atmospheric imaging results from the Mars Exploration Rovers: Spirit and Opportunity, *Science*, *306*, 1753–1756, doi:10.1126/science.1104474.
- Lichtenberg, K. A., et al. (2007), Coordinated analyses of orbital and Spirit rover data to characterize surface materials on the cratered plains of Gusev Crater, Mars, *J. Geophys. Res.*, *112*, E12S90, doi:10.1029/2006JE002850.
- Martinez-Alonso, S., B. M. Jakosky, M. T. Mellon, and N. E. Putzig (2005), A volcanic interpretation of Gusev Crater surface materials from thermophysical, spectral, and morphological evidence, *J. Geophys. Res.*, *110*, E01,003, doi:10.1029/2004JE002327.
- McGlynn, I. O., C. M. Fedo, and H. Y. McSween (2011), Origin of basaltic soils at Gusev Crater, Mars, by aeolian modification of impact-generated sediment, *J. Geophys. Res.*, *116*, E00F22, doi:10.1029/2010JE003712.
- McGuire, A., and B. Hapke (1995), An experimental study of light scattering by large irregular particles, *Icarus*, *113*, 134–155, doi:10.1006/icar.1995.1012.

- McLennan, S., et al. (2005), Provenance and diagenesis of the evaporite-bearing Burns formation, Meridiani Planum, Mars, *Earth and Planetary Science Letters*, *240*(1), 95 – 121, doi:http://dx.doi.org/10.1016/j.epsl.2005.09.041, <ce:title>Sedimentary Geology at Meridiani Planum, Mars</ce:title>.
- McSween, H. Y., et al. (2006), Characterization and petrologic interpretation of olivine-rich basalts at Gusev Crater, Mars, *Journal of Geophysical Research: Planets*, *111*(E2), n/a–n/a, doi:10.1029/2005JE002477.
- Milam, K. A., K. R. Stockstill, J. E. Moersch, J. McSween, Harry Y., L. L. Tornabene, A. Ghosh, M. B. Wyatt, and P. R. Christensen (2003), THEMIS characterization of the MER Gusev Crater landing site, *J. Geophys. Res.*, *108*, E12,8078, doi:10.1029/2002JE002023.
- Mosegaard, K., and A. Tarantola (1995), Monte Carlo sampling of solutions to inverse problems, *J. Geophys. Res.*, *100*, 12,431–12,447, doi:10.1029/94JB03097.
- Murchie, S. (2012), CRISM on MRO - instrument and investigation overview, in *MRO/CRISM Data Users' Workshop, The Woodlands, TX*.
- Murchie, S. et al. (2007), Compact Reconnaissance Imaging Spectrometer for Mars (CRISM) on Mars Reconnaissance Orbiter MRO, *J. Geophys. Res.*, *112*, E05S03, doi:10.1029/2006JE002682.
- Piatek, J., B. Hapke, R. Nelson, W. Smythe, and A. Hale (2004), Scattering properties of planetary regolith analogs, *Icarus*, *171*, 531–545, doi:10.1016/j.icarus.2004.05.019.
- Pilorget, C., M. Vincendon, and F. Poulet (2013), A radiative transfer model to simulate light scattering in a compact granular medium using a Monte-Carlo approach: Validation and first applications, *Journal of Geophysical Research: Planets*, pp. n/a–n/a, doi:10.1002/2013JE004465.
- Pilorget, C., J. Fernando, B. L. Ehlmann, and S. Douté (in preparation for *Icarus*), Photometry of particulate mixtures: what controls the phase curve?, *Icarus*.
- Pinet, P. C., et al. (2005), Derivation of Mars surface scattering properties from OMEGA spot pointing, *Lunar Planet. Sci.*, *XXXVI*, abstract 1694.
- Pollack, J. B., O. B. Toon, and B. N. Khare (1973), Optical properties of some terrestrial rocks and glasses, *Icarus*, *19*(3), 372 – 389, doi:http://dx.doi.org/10.1016/0019-1035(73)90115-2.
- Pommerol, A., N. Thomas, B. Jost, P. Beck, C. Okubo, and A. McEwen (2013), Photometric properties of Mars soils analogs, *J. Geophys. Res.*
- Poulet, F., C. Gomez, J.-P. Bibring, Y. Lanagan, B. Gondet, P. Pinet, and J. Belluci, G. Mustard (2007), Martian surface mineralogy from Observation pour la Mineralogie, l'Eau, les Glaces et l'Activite on board the Mars Express spacecraft (OMEGA/MEx): Global mineral maps, *J. Geophys. Res.*, *112*, E08S02, doi:10.1029/2006JE002840.
- Roush, T. L., F. Esposito, G. R. Rossman, and L. Colangeli (2007), Estimated optical constants of gypsum in the regions of weak absorptions: Application of scattering theories and comparisons to independent measurements, *Journal of Geophysical Research: Planets*, *112*(E10), n/a–n/a, doi:10.1029/2007JE002920.
- Shaw, A., M. J. Wolff, F. P. Seelos, S. M. Wiseman, and S. Cull (2013), Surface scattering properties at the Opportunity mars rover's traverse region measured by CRISM, *Journal of Geophysical Research: Planets*, *118*(8), 1699–1717, doi: 10.1002/jgre.20119.
- Shepard, M. K., and P. Helfenstein (2007), A test of the Hapke photometric model, *J. Geophys. Res.*, *112*, E03,001, doi:10.1029/2005JE002625.
- Shkuratov, Y. G., D. G. Stankevich, D. V. Petrov, P. C. Pinet, A. M. Cord, Y. H. Daydou, and S. D. Chevrel (2005), Interpreting photometry of regolith-like surfaces with different topographies, *Icarus*, *173*, 3-15, doi:10.1016/j.icarus.2003.12.017.
- Soderblom, L. A., et al. (2004), Soils of Eagle Crater and Meridiani Planum at the Opportunity rover landing site, *Science*, *306*, 1723, doi:10.1126/science.1105127.
- Sokolik, I. N., and O. B. Toon (1999), Incorporation of mineralogical composition into models of the radiative properties of mineral aerosol from UV to IR wavelengths, *Journal of Geophysical Research: Atmospheres*, *104*(D8), 9423-9444, doi:10.1029/1998JD200048.

- Souchon, A. L., P. Pinet, S. Chevrel, Y. Daydou, D. Baratoux, K. Kurita, M. K. Shepard, and P. Helfenstein (2011), An experimental study of Hapke's modeling of natural granular surface samples, *Icarus*, *215*, 313–331, doi:10.1016/j.icarus.2011.06.023.
- Squyres, S. W., et al. (2004a), The Spirit rover's Athena Science Investigation at Gusev Crater, Mars, *Science*, *305*, 794, doi:10.1126/science.3050794.
- Squyres, S. W., et al. (2004b), The Opportunity rover's Athena Science Investigation at Meridiani Planum, Mars, *Science*, *306*, 1698, doi:10.1126/science.1106171.
- Squyres, S. W., et al. (2004c), In situ evidence for an ancient aqueous environment at Meridiani Planum, Mars, *Science*, *306*(5702), 1709–1714, doi:10.1126/science.1104559.
- Squyres, S. W., et al. (2006), Overview of the Opportunity Mars Exploration Rover mission to Meridiani Planum: Eagle Crater to Purgatory Ripple, *J. Geophys. Res.*, *111*, E12S12, doi:10.1029/2006JE002771.
- Squyres, S. W. et al. (2006), Two years at Meridiani Planum: Results from the Opportunity rover, *Science*, *313*, 1403, doi:10.1126/science.1130890.
- Sullivan, R., et al. (2005), Aeolian processes at the Mars Exploration Rover Meridiani Planum landing site, *Nature*, *436*, 58–61, doi:10.1038/nature03641.
- Sullivan, R., et al. (2008), Wind-driven particle mobility on Mars: Insights from Mars Exploration Rover observations at "El Dorado" and surroundings at Gusev Crater, *Journal of Geophysical Research: Planets*, *113*(E6), doi:10.1029/2008JE003101.
- Tarantola, A., and B. Valette (1982), Inverse problems=quest for information, *J. Geophys.*, *50*, 159–170.
- Thomas, P., J. Veverka, D. Gineris, and L. Wong (1984), "dust" streaks on Mars, *Icarus*, *58*, 331–338.
- Tomasko, M. G., L. R. Dose, M. Lemmon, P. H. Smith, and E. Wegryn (1999), Properties of dust in the Martian atmosphere from the imager on Mars Pathfinder, *Journal of Geophysical Research: Planets*, *104*(E4), 8987–9007, doi:10.1029/1998JE900016.
- Vaughan, A., J. Johnson, K. E. Herkenhoff, R. Sullivan, G. A. Landis, W. Goetz, and M. B. Madsen (2010), Pancam and Microscopic Imager observations of dust on the Spirit rover: Cleaning events, spectral properties, and aggregates, *Mars*, *5*, pp. 129–145.
- Ward, J. G., R. E. Arvidson, and M. Golombek (2005), The size-frequency and areal distribution of rock clasts at the Spirit landing site, Gusev Crater, Mars, *Geophys. Res. Lett.*, *32*, L11,203, doi:10.1029/2005GL022705.
- Weitz, C. M., et al. (2006), Soil grain analyses at Meridiani Planum, Mars, *J. Geophys. Res.*, *111*, E12S04, doi:10.1029/2005JE002541.
- Wolff, M. J., M. D. Smith, R. T. Clancy, R. Arvidson, M. Kahre, F. Seelos, S. Murchie, and H. Savijarvi (2009), Wavelength dependence of dust aerosol single scattering albedo as observed by the Compact Reconnaissance Imaging Spectrometer, *J. Geophys. Res.*, *114*, E00D64, doi:doi:10.1029/2009JE003350.
- Wray, J. J., E. Z. Noe Dobrea, R. E. Arvidson, S. M. Wiseman, S. W. Squyres, A. S. McEwen, J. F. Mustard, and S. L. Murchie (2009), Phyllosilicates and sulfates at Endeavour Crater, Meridiani Planum, Mars, *Geophysical Research Letters*, *36*(21), n/a–n/a, doi:10.1029/2009GL040734.